



Early Diagenesis of Lacustrine Carbonates in Volcanic Settings: The Role of Magmatic CO₂ (Lake Dziani Dzaha, Mayotte, Indian Ocean)

Vincent Milesi, Mathieu Debure, Nicolas C.M. Marty, Manuela Capano, Didier Jézéquel, Carl Steefel, Virgile Rouchon, Patrick Albéric, Edouard Bard, Gérard Sarazin, et al.

► To cite this version:

Vincent Milesi, Mathieu Debure, Nicolas C.M. Marty, Manuela Capano, Didier Jézéquel, et al.. Early Diagenesis of Lacustrine Carbonates in Volcanic Settings: The Role of Magmatic CO₂ (Lake Dziani Dzaha, Mayotte, Indian Ocean). ACS Earth and Space Chemistry, 2020, 4 (3), pp.363-378. 10.1021/acsearthspacechem.9b00279 . insu-02499121

HAL Id: insu-02499121

<https://insu.hal.science/insu-02499121>

Submitted on 4 May 2020

HAL is a multi-disciplinary open access archive for the deposit and dissemination of scientific research documents, whether they are published or not. The documents may come from teaching and research institutions in France or abroad, or from public or private research centers.

L'archive ouverte pluridisciplinaire **HAL**, est destinée au dépôt et à la diffusion de documents scientifiques de niveau recherche, publiés ou non, émanant des établissements d'enseignement et de recherche français ou étrangers, des laboratoires publics ou privés.

EARLY DIAGENESIS OF LACUSTRINE CARBONATES IN VOLCANIC SETTINGS: CHARACTERIZATION AND MODELING

VINCENT P. MILESI¹, MATHIEU DEBURE², NICOLAS C.M. MARTY², MANUELA
CAPANO³, DIDIER JÉZÉQUEL¹, CARL STEEFEL⁴, VIRGILE ROUCHON⁵, PATRICK
ALBÉRIC⁶, EDOUARD BARD³, GÉRARD SARAZIN¹, FRANÇOIS GUYOT⁷, AURÉLIEN
VIRGONE⁸, ÉRIC C. GAUCHER⁸ AND MAGALI ADER¹

¹Université de Paris, Institut de physique du globe de Paris, CNRS, F-75005 Paris, France,
vincentmilesi@hotmail.fr

²BRGM, French Geological Survey, Orléans, France

³Collège de France, CEREGE, Aix en Provence, France

⁴Lawrence Berkeley National Laboratory, USA

⁵IFP Energies Nouvelles, Direction Géosciences, Rueil-Malmaison, France

⁶Institut des Sciences de la Terre d'Orléans, Orléans, France

⁷IMPMC, Sorbonne Université, MNHN, Paris, France

⁸Total, EP CSTJF, Pau, France

The interplay of diagenetic processes in time and space makes quantitative assessments for paleoenvironmental reconstructions and reservoirs property predictions difficult. We studied the first meter of carbonate sediments of the Dziani volcanic crater lake (Mayotte Island), seen as an analog of lacustrine carbonates formed in rift settings and developed a new reactive-transport model with the Crunchflow code, which allows the quantification of diagenetic reactions by considering burial rate and sediment compaction. The model is constrained by the already-known solid phase composition of the lake sediment and by a series of new data: ^{14}C dating of plant macro-remains to characterize the sediment age model, chemical composition of sediment pore waters and chemical and isotopic composition of gases dissolved and bubbling through the lake. These new data reveal a massive magmatic CO_2 contribution to the dissolved inorganic carbon of the lake, which fuels the primary productivity and the carbonate formation. The intense primary productivity raises the lake water pH above 9, inducing supersaturations of the surface sediment pore waters relative to aragonite, hydromagnesite and saponite. The model allows quantifying the contributions of microbial degradation of organic matter and magmatic CO_2 inflows (2 mol.% and 22 mol.% at 1 m depth, respectively) to the dissolved inorganic carbon of sediment pore waters. These magmatic CO_2 inflows induce a pH decrease at depth, leading to the destabilization of hydromagnesite while saponite and aragonite remains stable. These results bring new insights on the origin and diagenetic evolution of lacustrine carbonates in rift settings. They demonstrate the possible role of magmatic CO_2 in setting the chemical conditions required for the co-precipitation of carbonate and Mg-silicates, in fueling the carbonate production, and in controlling the diagenetic evolution of the sediment mineralogy.

Keywords: magnesium phyllosilicates, rift settings, reactive transport modeling, kinetics, magmatic CO_2 , saponite, isotopy, Dziani Dzaha, volcanic crater lake

1. Introduction

Diagenetic processes are an important feature of the functioning of the Earth system, from the reconstruction of paleoenvironments and biogeochemical cycles to the prediction of sedimentary rocks porosity and permeability. The diagenesis of reactive minerals, such as carbonates, is an especially complex system as both chemical and physical processes occur concurrently. In addition to compaction during burial, diagenetic evolution of carbonate-bearing rocks can be affected by dolomitization and dedolomitization^{1,2}, carbonate cementation³, acidic fluids inputs^{4,5}, dissolution of associated magnesium phyllosilicates⁶⁻⁸, and bacterial and thermal sulphate reduction⁹ among others. Thus, the outcomes of diagenesis are the results of a combination of processes occurring simultaneously or successively and in various extents depending on the initial sediment composition, the nature of the pore fluids, and the pressure and temperature conditions¹⁰. One of the main

challenges to further improve our understanding of the depositional and post depositional conditions leading to sedimentary rocks is to quantify how diagenetic processes interact together in time and space.

Numerical models allow exploring the highly nonlinear coupling that characterizes natural systems. It allows quantitative evaluation of the coupling between physical, chemical, and biological processes that control Earth surface systems^{11,12}. Relying on thermodynamics and kinetics constants available for an increasing number of reactions^{13–16}, reactive transport codes can be used to perform forward modeling of compositional changes of fluid and solid phases of sedimentary columns as burial and fluid circulation occur^{10,17–20}. Because of the chemical reactivity of carbonates, this approach is especially valuable for paleoenvironmental interpretations of carbonate sediments which are among the most abundant and widely used archives of Earth chemical and climatic history^{21–23}.

Cretaceous pre-salt carbonates of the South Atlantic continental margins and Proterozoic carbonates of the Ediacaran Doushantuo formation have been the focused of many studies of paleoenvironmental reconstruction in recent years^{6–8,22,24–28}. Pre-salt carbonate rocks contain some of the most significant petroleum reservoirs discovered in decades while the Ediacaran formation (635 to 551 Ma) hosts the earliest animal fossils in the geological record. In both formations, carbonates are associated with Mg-phyllsilicates; however, the sources of magnesium, silica and high pH values required for the Mg-phyllsilicates formation remain unclear, preventing accurate paleoenvironmental reconstruction^{8,22,24,27,29,30}. Questions remain on the initial mineralogy of the Ca-carbonates and on the source of carbon capable of producing carbonates in lacustrine environments with the volume and the spatial extent of the pre-salt carbonates^{28,29}.

The geochemical and sedimentological study of contemporaneous analogs of those paleoenvironments, coupled with quantitative diagenetic models, is a method to assess these questions. In this contribution, we studied the first meter of carbonate sediments of the Dziani Dzaha volcanic crater lake (Mayotte Island), seen as a good analog of lacustrine environments in the early stages of continental rifting during which low mantle uplift results in low partial melting, producing alkaline magma^{31,32}. The Dziani Dzaha sediment, previously characterized in detail by Milesi *et al.*³³, shows significant compositional changes with depth, with a decrease of hydromagnesite and organic matter and a simultaneous increase of a Mg- and Al-rich smectite characterized as a saponite-like mineral (referred hereafter as saponite). The pore water chemistry, the chemical and carbon isotopic composition of gases bubbling through the lake, the concentration of CH₄ dissolved in the lake water, and ¹⁴C dating of plant macro-remains in the sediment cores were acquired to develop a fully-constrained reactive transport model of the diagenetic processes at play. The model accounts for the fluid and solid burial as well as the sediment compaction with time. The early diagenesis is a stage of considerable compositional changes due to the interplay of biological, chemical and physical

processes³⁴. Our study focuses on those processes, which are the foundation toward modeling further diagenetic stages in larger-scale basins.

2. Geologic setting and limnology of the Dziani Dzaha

The Dziani Dzaha is a tropical crater lake located on the island complex of Mayotte, which is the most southern island complex of the Comoros Archipelago (western Indian Ocean). The island of Petite Terre results from the most recent magmatic events in the Mayotte history, starting 80,000 years ago. It is made primarily of pyroclastic rocks of phonolitic/alkaline composition produced by partial melting of the lithospheric mantle metasomatized by CO₂-rich fluids^{35,36}. The Dziani Dzaha is hosted in a volcanic crater formed by a phreatomagmatic eruption, which may correspond to one of the most recent volcanic events of the island of Petite Terre dated from 9 Ka to 4 Ka³⁷.

The lake is meromictic. It is approximately at sea level, with an average depth of 3.5 m, and a singular depression down to 18 m where the water does not intermix (monimolimnion layer) (Fig. 1). Four sites of volcanic gas bubbling are identified within the lake associated with microbialites mainly made of calcite and aragonite³⁸. The lake water has a salinity ranging from 34 and 71 g·kg⁻¹ depending on the season and depth (*i.e.*, between once and twice seawater's salinity), alkalinity of ~0.2 mol·L⁻¹ and pH values ranging from 9.1 to 9.4. The surface temperature varies between 28 and 36°C. Together, these characteristics correspond to the thalassohaline lake definition³⁹. The lake biomass is dominated by cyanobacteria, with a primary productivity of ~8 g of C·m⁻²·day⁻¹³⁹, close to the maximum rate of photosynthesis for tropical and subtropical lakes⁴⁰. The most likely theory of the lake origin is sea water filling the volcanic crater formed by the phreatomagmatic eruption³⁹. The limnigraphic measurements performed since 2014 show a balanced hydrologic budget. The lake water level is constant, with maxima reached from December to February and minima from Mai to September. Contribution of seawater inflows pulsed by tidal waves to the hydrologic budget can be ruled out as, even mitigated, they would have been recorded by the limnigraph considering its sensitivity (±10 mm) and the magnitude of the tidal waves (3 m). The absence of external water inflows is confirmed by the concentration of the conservative elements, Cl and Br which are not involve in any biogeochemical processes. The Cl/Br ratio of the lake water is within 10% equal to that of seawater (Table S1). Therefore, the Cl_{lake}/Cl_{seawater} ratio of ca. 1.7 can be attributed to the lack of meteoric inputs compared with evaporation over the life time of the lake (Table S1). Given this preliminary interpretation of the lake origin and functioning (further investigations in progress), the massive photosynthetic activity in the lake is the most likely process at the origin of the high pHs.

The uppermost sediment of the Dziani Dzaha is dominated by organic matter and the authigenic carbonates, aragonite and hydromagnesite³³. With increasing depth, the content of

hydromagnesite decreases while the one of saponite increases. Over the same interval, the organic matter which represents up to 40wt.% of the uppermost sediment in the deep parts of the lake decreases to 25-30wt.% at 1 m depth. Detrital inputs made of alkaline feldspar, clinopyroxene and volcanic pumice are present along the first meter of sediment. This mineral composition is observed in all sediment cores collected between 2 to 5 meters of water depth.

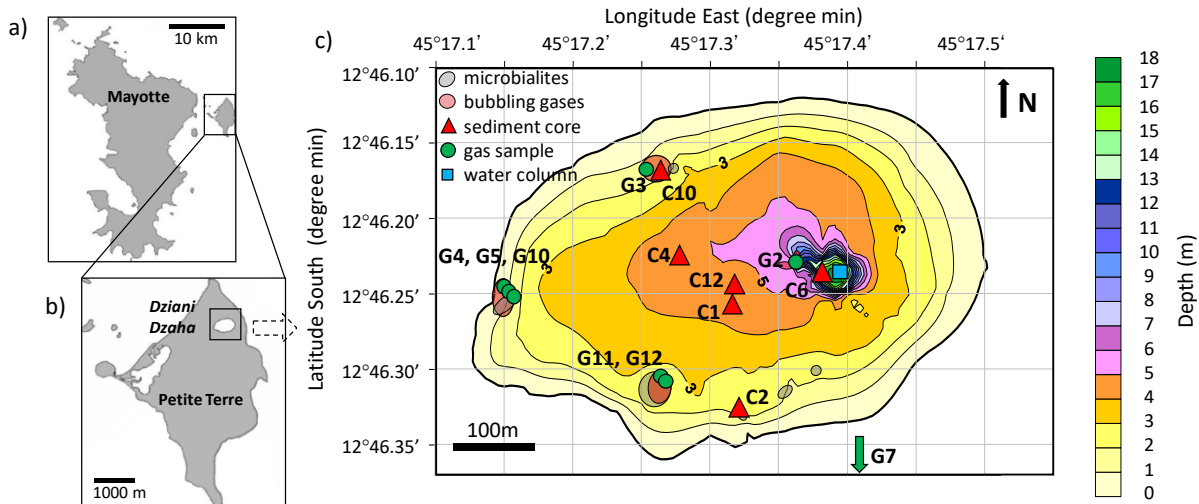


Figure 1. (a and b) Situation map of the study site (modified from the study of Milesi *et al.*³³). (c) Bathymetric map of the Dziani Dzaha showing bubbling sites (light red circles), microbialites (light grey circles), sites of sediment core sampling (CX, red triangles), sampled water column (blue square) and bubbling gases (GX, green circles).

3. Material and Method

3.1 Nomenclature

All samples are named as follows. For DZ14-10 C4, “DZ” is for Dziani, “14-10” is for the year (2014) and month (October) of the survey and C4 refers to the sediment core 4. In this nomenclature, “C” stands for sediment core, “G” for gas sample and “WC” for water column. The samples are listed in Table S2 in supporting information. As the sediment cores and the gas samples were named according to their sampling order, they are named in Figure 1 and in the article only as CX and GX, with X the number of the sample.

3.2 Sampling

The pore waters of sediment core C12 were sampled with Rhizon samplers during the survey of August 2016. The porous tubes with a mean pore size of 0.15 μm were placed every 2.5 cm along the 1 m long sediment core and connected to 12 mL-evacuated Exetainer[®] vials or to plastic syringes in order to avoid silicon contamination from the Exetainer[®] glass. Within a few hours after collection, the 27 pore water samples were acidified with high purity HNO_3 for ulterior analysis of major cations concentrations.

The water column was sampled above the 18 m depression of the lake with a Niskin[®] bottle during the surveys of September 2010, 2011, April 2012, 2014 and August 2016. The lake waters were stored in 12 mL Exetainer[®] vials filled with water (no headspace) and poisoned with mercuric chloride (HgCl_2) to prevent microbial activity.

Radiocarbon measurements were performed on dissolved inorganic carbon (DIC), particulate organic carbon (POC), sediment inorganic carbon (SIC), sediment organic carbon (SOC) and on terrestrial plants macro-remains. Dissolved inorganic carbon (DIC) was sampled as Ba-precipitates. At field, a solution of concentrated Ba-hydroxide is introduced into headspace-free sampling bottles (1L), causing the precipitation of DIC as Ba-carbonates which are later filtered (glass fiber filter grade GF/C $\approx 1.2\mu\text{m}$) and dried under an atmosphere free of CO_2 . Particulate organic carbon (POC) was sampled by filtration of water on GF/F glass fiber filters ($\approx 0.7\mu\text{m}$).

For the sampling of gases bubbling at the lake surface (survey of August 2016), 12 mL Exetainer[®] vials were filled with the lake water and then flushed with the bubbling gases until water is completely removed. Contamination from atmosphere is carefully avoided by constantly keeping the vials under the water level during sampling.

3.3 Chemical and isotopic composition of pore waters and gas samples

The pH values of pore waters were measured within a few hours after sampling. Major cations were analyzed at the IPGP laboratory with inductively-coupled plasma atomic emission spectroscopy (ICP-AES). Sulfate, H₂S and CH₄ were not measured because of the difficulty of avoiding the degassing and oxidation of H₂S and CH₄ during the sediment core collection and during the sampling and storage of the pore waters.

The carbon and hydrogen isotope composition of CH₄ and CO₂ of bubbling gases and of pore waters were analyzed at the IFPEN laboratory by sampling directly the headspaces of Exetainer® vials. CH₄ and CO₂ were separated by on-line gas chromatography and their carbon and hydrogen isotope-ratios were measured by mass spectrometry. Isotopic compositions are reported relative to the Pee Dee belemnite (PDB) standard for carbon and relative to the Standard Mean Ocean Water for hydrogen (SMOW). Precisions for isotopic compositions are of ±1‰ for δ¹³C and ±5‰ for δD.

The concentration of CO₂ and CH₄ dissolved in the water column was measured at the IFPEN laboratory after splitting the water samples in two parts in order to create headspaces in the Exetainer® vials (a syringe is introduced through the septa to transfer the liquid from one vial to another). After 48h of equilibration, the gas phase was sampled with a gas tight syringe and injected in a gas chromatograph connected to a thermal conductivity detector and a flame ionization detector, allowing quantification of H₂, He, CO₂, O₂, N₂, and all hydrocarbons from methane to iso- and normal-butane. Precisions for individual components are ±2%. The concentrations of dissolved methane and CO₂ were calculated considering gas/solution equilibrium.

3.4 Porosity profile and density calculations

The water content was estimated in the sediment core C12 by weighting 29 fresh samples before and after drying (80°C). The measurements were corrected for the precipitation of halite (NaCl) during drying, using the pore water salinity and the water content to calculate the amount of precipitated halite. As no data was available for the sediment composition of the core C12, the density of the dried sediment was calculated using the organic matter and mineral contents of the sediment core C4 and C10³³. This approach is reasonable given the steady sediment composition between cores collected close to one another³³. The densities for aragonite, hydromagnesite, alkaline feldspar, clinopyroxene, saponite, organic matter, halite, pyrite and magnetite are taken to be 2.9, 2.2, 2.6, 3.2, 2.5, 0.8, 2.2, 5.0 and 5.2 kg·m⁻³, respectively.

3.5 Radiocarbon measurements

Water column and bulk sediment samples were analyzed by accelerator mass spectrometry (AMS) at the LMC14 Artemis AMS facility (CEA Saclay - Gif/Yvette, France). Dissolved and sediment

inorganic carbon (DIC as Ba-carbonates and SIC, respectively) were extracted at 60°C by adding anhydrous H₃PO₄ until complete CO₂ outgassing occurred. For particulate and sediment organic carbon (POC and SOC, respectively), the samples were acidified (0.5M HCl, 80°C, 1 hour) to remove the carbonates and rinsed with deionized water. POC and SOC were then converted to CO₂ at 900°C during 4 hours in contact with Cu-oxides and a wire of Ag. The ¹⁴C activities are reported relative to the oxalic acid standard HOxII and normalized to a δ¹³C value of -25‰. Radiocarbon ages and Delta notations are calculated according to the studies by Mook and van der Plicht⁴¹ and Stuiver and Polach^{42,43}, respectively.

Terrestrial plant macro-remains were analyzed by means of Aix-MICADAS AMS facility of Aix-en-Provence⁴⁴. The samples were treated with a modified ABA chemical pretreatment to avoid possible contaminations from the lake DIC, carbonates and organic carbon⁴⁵. Standards (OxA2 NIST SRM4990C) and blanks (VIRI K) were analyzed together with samples. The ¹⁴C data are reported in terms of conventional ¹⁴C age in years BP and in F¹⁴C^{42,46,47}.

3.6 Reactive transport modeling

The CrunchFlow multicomponent reactive transport code⁴⁸ was used with the Thermoddem database^{13,14} to model the early diagenesis of the sediment. The model accounts for kinetic and thermodynamic chemical processes (water/rock interaction), diffusive transport, together with fluid and sediment burial and compaction with time.

3.6.1 Solid and fluid burial

Sediment compaction depends on the time-scale, the stress, the pressure, the temperature and the rheology of the sediments^{17,49}. The downward advection of the pore water (*i.e.*, fluid burial rate) is identical to the burial rate of solids relative to the water-sediment interface only if the compaction is negligible and if there is no external driving force for the fluid (such as upwelling from hydrothermal vents or lateral fluid flow). Compaction over long time scales in fine-grained sediments results in non-constant pore water and solid burial rates that can produce appreciable changes in the water content, and therefore, in the chemical profiles¹¹. For instance, reaction-generated grain-scale permeability is sealed rapidly by compaction, which prevents or at least reduces fluid fluxes⁴⁹.

The solid burial rate, ω , can be determined from the conservation of solid sediment mass (where ϕ is the porosity and z is the depth (m)) as follow^{11,17}:

$$\frac{\partial[(1-\phi)\omega]}{\partial z} = 0 \quad \text{Eqs (1)}$$

The fluid flow due to compaction, v , can be determined from the conservation of fluid mass given the assumption of steady-state compaction:

$$\frac{\partial(\phi v)}{\partial z} = 0 \quad \text{Eqs (2)}$$

The porosity profile ϕ as a function of the depth z was fitted in this study assuming that the dissolution/precipitation mechanisms influence the porosity. Considering the asymptotic burial rate of fluid and solid as boundary condition, the equations (1) and (2) become respectively:

$$\omega = \frac{W(1-\phi_{bottom})}{1-\phi_z}, \quad \text{Eqs (3)}$$

$$v = \frac{W\phi_{bottom}}{\phi_z}, \quad \text{Eqs (4)}$$

with ϕ_z the porosity at a given depth z and ϕ_{bottom} and W the porosity and the asymptotic burial rate, respectively. Then, solid and fluid burial rates were calculated by solving numerically the equations (3) and (4) using the expression of the porosity profile. The fluid and solid burial rates are considered asymptotic at 5 m depth, which, according to most recent coring, is the approximated depth of the volcanic basement. The value of the asymptotic burial rate at 5 m depth (W) was adjusted for the calculated solid burial rate to fit at best the sedimentation rate determined using the plant macro-remains ages.

3.6.2 Minerals, organic matter and associated reactions

The sediment composition is dominated by organic matter and authigenic minerals (aragonite, hydromagnesite and Mg-rich saponite) with lower amounts of detrital silicates, mostly clinopyroxenes and alkaline feldspars with a chemical composition close to the one of anorthoclase ($\text{Na}_{0.7}\text{K}_{0.3}\text{Si}_3\text{O}_8$)³³. Accordingly, albite, diopside, aragonite, hydromagnesite, dolomite, gibbsite, quartz, microcline and Mg-rich saponite are considered in the model. Those minerals may either precipitate or dissolve depending on the saturation state of the pore waters. The reaction kinetics R ($\text{mol}\cdot\text{s}^{-1}$) are described according to the TST rate law⁵⁰⁻⁵³ as:

$$R = A * k * e^{\frac{-E_a}{RT}} \prod a_i^n (1 - (\frac{Q}{K})^\theta)^\eta \quad \text{Eqs (5)}$$

where A is the mineral surface area ($\text{m}^2\cdot\text{g}^{-1}$), k is the intrinsic rate constant ($\text{mol}\cdot\text{m}^{-2}\cdot\text{s}^{-1}$), E_a is the activation energy ($\text{kcal}\cdot\text{mol}^{-1}$), R is the gas constant ($\text{J}\cdot\text{K}^{-1}\cdot\text{mol}^{-1}$), T is the temperature in Kelvin, $\prod a_i^n$ is a product of the activities a of various ions i in solution raised to the power n , which represents the inhibition or catalysis of the reaction by these ions. Especially, it allows considering a dependence of the reaction on pH. Q is the ion activity product for the mineral-water reaction, K is the corresponding equilibrium constant, θ and η are empirical parameters describing the affinity dependence of the reaction. The thermodynamic and kinetic parameters for minerals are based on literature values (Table 1). The rate constant of Mg-saponite is adjusted to fit the observation as no data exists in the literature.

The organic matter is treated as a solid phase with a simplified stoichiometry of CH₂O. The mineralization of the organic matter is represented by a reaction that describes a simplified process of microbial methanogenesis coupled to microbial fermentation (Table 1). This approach relies on the observation of high densities of methanogens and heterotrophs in the lake waters³⁹.

Table 1. Thermodynamic and kinetic parameters of the modeled reactions

Solid phases	Reaction stoichiometry	log K* (25°C)	log k** (mol·m ⁻² ·s ⁻¹)	Surface area (m ² ·g ⁻¹)	Activation energy (kcal·mol ⁻¹)	Ion activity dependence [§] (i, n)	Affinity dependence ^{§§} (θ, η)
Organic matter	2CH ₂ O → CO ₂ + CH ₄	10	-10.3 ⁵⁴	1.5 ⁵⁵	0		1, 1
Albite	NaAlSi ₃ O ₈ + 4H ⁺ + 4H ₂ O Al ³⁺ + Na ⁺ + 3H ₄ SiO _{4(aq)}	2.9962 ⁵⁶	-9.85 ¹⁵	0.6 ⁵⁷	13.4 ¹⁵	OH ⁻ 0.32 ¹⁵ / none	0.48, 100 ¹⁵ / 1, 1
Microcline	KAlSi ₃ O ₈ + 4H ⁺ + 4H ₂ O = Al ³⁺ + K ⁺ + 3H ₄ SiO _{4(aq)}	0.0036 ⁵⁶	-9.85 ^{based on 15}	0.6 ⁵⁷	13.4 ^{based on 15}		1, 1
Diopside	CaMgSi ₂ O ₆ + 4H ⁺ + 2H ₂ O = Ca ²⁺ + Mg ²⁺ + 2H ₄ SiO _{4(aq)}	21.7345 ⁵⁸	-9.54 ⁵⁹	3 ⁵⁷	9.7 ⁵⁹	H ⁺ 0.18 ⁵⁹	1, 1
Quartz	SiO ₂ + 2H ₂ O = H ₄ SiO _{4(aq)}	-3.7372 ⁶⁰	-9.72 [°] / -11.49 ¹⁵	0.2 ¹⁵	19.12 ¹⁵ / 11.95 ¹⁵	OH ⁻ 0.34 ¹⁵ / none	1, 1 / 4.58, 0.54 ¹⁵
Gibbsite	Al(OH) ₃ + 3H ⁺ = Al ³⁺ + 3H ₂ O	7.7341 ⁶¹	-5.51 ¹⁵	1 ¹⁵	11.5 ¹⁵	OH ⁻ 1.0 ¹⁵	1, 1
Aragonite	CaCO ₃ + H ⁺ = Ca ²⁺ + HCO ₃ ⁻	2.0143 ⁶²	-5.57 ⁶³ / -7.65 ⁶⁴	0.1 ⁶⁵	0 / 17.02 ⁶⁴		1, 0.86 ⁶³ / 1, 1.7 ⁶⁴
Hydromagnesite	Mg ₅ (OH) ₂ (CO ₃) ₄ ·4H ₂ O + 6H ⁺ = 4HCO ₃ ⁻ + 5Mg ²⁺ + 6H ₂ O	31.3922 ⁶⁶	-10.39 ⁶⁷	1.0 ⁶⁷	10.87 ⁶⁷		0.2, 1 ⁶⁷
Dolomite	CaMg(CO ₃) ₂ + 2H ⁺ = 2HCO ₃ ⁻ + Ca ²⁺ + Mg ²⁺	3.5328 ⁶⁶	-7.96 ¹⁵ / -14.02 ¹⁵	0.1 ¹⁵	7.41 ¹⁵ / 24.61 ¹⁵		0.16, 2.1 ¹⁵ / 1, 1
Saponite	Mg _{0.17} Mg ₃ Al _{0.34} Si _{3.60} O ₁₀ (OH) ₂ + 7.36H ⁺ = 2.64H ₂ O + 0.34Al ³⁺ + 3.17Mg ²⁺ + 3.66H ₄ SiO _{4(aq)}	28.7937 ¹⁴	-18 ¹	150 ⁶⁸⁻⁷¹	14.58 ^{based on 15}		1, 1

Values on the left and right side of the slash symbol are for dissolution and precipitation reactions, respectively. In case of single value, the value is used for both dissolution and precipitation reactions.

*K is the equilibrium constant of the reaction. Thermodynamic data are from the Thermoddem database (Blanc et al., 2012).

**k is the intrinsic rate constant.

§The first term i is the ion in solution, the second term n is the power to which the activity of ion i is raised.

§§The first and second term are the empirical parameters θ and η describing the affinity dependence.

†fitted with the observation

3.6.3 Model conditions and parameters

The model domain consists of a one-dimensional column of sediment with a Dirichlet-type boundary condition at the sediment-water interface (infinite reservoir with constant concentrations for dissolved species and constant volume fractions for solids), and a pure advective, no diffusive flux boundary condition at the bottom (1 m depth) (Fig. 2). A fixed grid of 1 m height is used, made of 200 cells with a constant grid spacing of 5 mm. Initially, the entire column is free of organic matter or minerals and filled with the surface porewater charge balanced with chloride (Table 2). The aluminum concentration is set at equilibrium with gibbsite. Iron was not considered which appears reasonable considering its low concentrations in pore waters (mostly <50μM) and the absence of significant amounts of iron bearing mineral in the sediments³³. The Dirichlet-type boundary condition at the sediment-water interface allows modeling constant inputs of water, minerals and organic matter from the lake to the sediment column. The supplied water has a constant composition equal to the one of surface pore waters. The volume fraction of supplied minerals and organic matter at the Dirichlet-type boundary condition is adjusted to fit the observations (Table 2). In addition to albite and diopside, an input of hydromagnesite is considered as it is expected to precipitate in the lake-water column or at the

sediment surface due to its supersaturation in the lake water. Fluids and solids are supplied to the sediment column considering the calculated burial rate and water diffusion. There are no additional transport processes such as advection, therefore no permeability value is required in the model. The initial porosity of 100% (column free of solid phases) is updated at each calculation step as minerals and organic matter are brought from the sediment-water interface and precipitate or dissolve during the calculation. At the flux boundary condition (bottom of the sediment column), an injection of CO₂ is considered. The gas flow rate is adjusted to fit the pH profile. The temperature, pressure, and pore diffusion coefficient are fixed at 30°C, 1 bar, and $2 \cdot 10^{-9} \text{ m}^2 \cdot \text{s}^{-1}$, respectively. Each simulation was run for 4000 years, which corresponds to the estimation of the youngest age of the lake formation³⁷ and is equal to 4 times the approximate age of the sediment at 1 m depth. This results in the sediment from the sediment-water interface moving completely through the column, thus achieving quasi-steady state results.

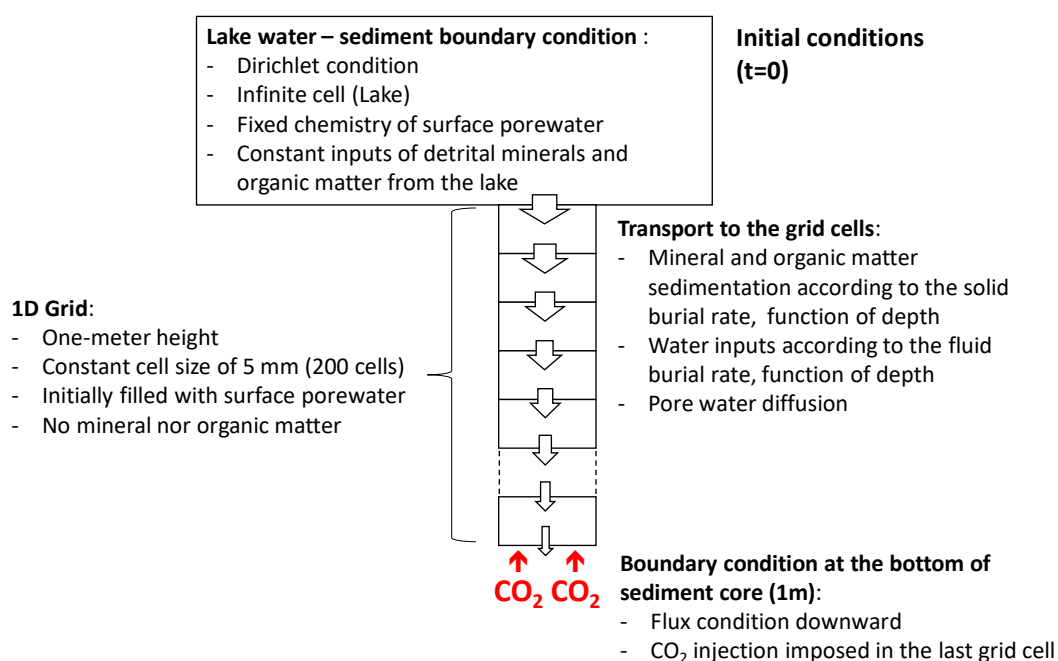


Figure 2. Schematic diagram of the reactive transport model.

Table 2. Boundary conditions of the reactive transport model at the sediment-water interface

Water		Organic matter and minerals	
-	Concentration (mol·kg ⁻¹)	-	Volume fraction (m ³ ·m ⁻³)
Temperature (°C)	30	Organic matter	0.0038
pH	9	Albite	0.003
HCO ₃ ⁻	2·10 ⁻¹	Diopside	0.001
Cl ⁻	charge balanced	Hydromagnesite	0.0015
Na ⁺	0.95		
K ⁺	3.5·10 ⁻²		
Mg ²⁺	4·10 ⁻³		
Ca ²⁺	1·10 ⁻⁴		
Al ³⁺	Gibbsite*		
SiO _{2(aq)}	1.7·10 ⁻⁴		
O _{2(aq)}	1·10 ⁻¹⁰		

4. *Al concentration set at equilibrium with gibbsite

Results

4.1 Dissolved and bubbling gases

The concentration of dissolved methane in the water column evolves along its saturation concentration, increasing with depth to reach 3180 μM at 18 m depth (Fig. 3, Table S3 in supporting information). The CO_2 concentration increases from 24 μM at surface to 263 μM at 18 m depth and remains ca. two orders of magnitude lower than its saturation concentration. Both concentrations of methane and CO_2 are orders of magnitude higher than their respective concentrations at equilibrium with atmosphere. In the pore waters, the $\delta^{13}\text{C}$ and $\delta^2\text{H}$ values of dissolved methane range between -72‰ and -62‰ and between -177‰ and -230‰, respectively (Fig. 4, Table S4 in supporting information), while dissolved CO_2 has $\delta^{13}\text{C}$ values between +2‰ and +7‰. The gases bubbling at the lake surface are mostly made of CO_2 , with minor amounts of N_2 , O_2 and CH_4 (Table 3). The samples G3, G4, G7 and G10 contain mostly CO_2 (>95 vol.%) with low amounts of methane (~0.3%). The $\delta^{13}\text{C}$ values of CO_2 and CH_4 gases range between 0 and -3‰, and between -17 and -11‰, respectively. The samples G5, G11 and G12 have similar chemical composition and $\delta^{13}\text{C}$ values of CO_2 but the $\delta^{13}\text{C}$ values of CH_4 are lower, ranging from -21 to -29‰. Sample G2 has a different chemical and isotopic composition. Methane represents 80 vol.% of the gas and its carbon isotope composition is of -66‰, close to the one of dissolved methane of pore waters. The CO_2 represents only 1.4 vol.% of the gases and its $\delta^{13}\text{C}$ value of -20‰ is lower than in other samples.

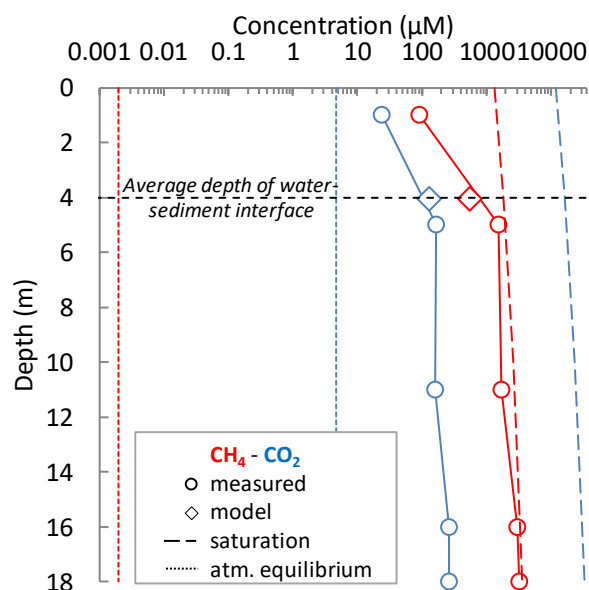


Figure 3. Concentration of dissolved methane and CO₂ in the water column straight up the 18 m depression (DZ14-4 WC). Methane and CO₂ data are in red and blue, respectively. The open circles are the measured concentrations. The modeled CO₂ and CH₄ concentrations in the first 10 cm of sediment are shown with open diamonds, at the average depth of the lake water – sediment interface. The dashed and dotted lines are the saturation concentrations and the concentrations at equilibrium with atmosphere, respectively. Calculation is done at 30°C.

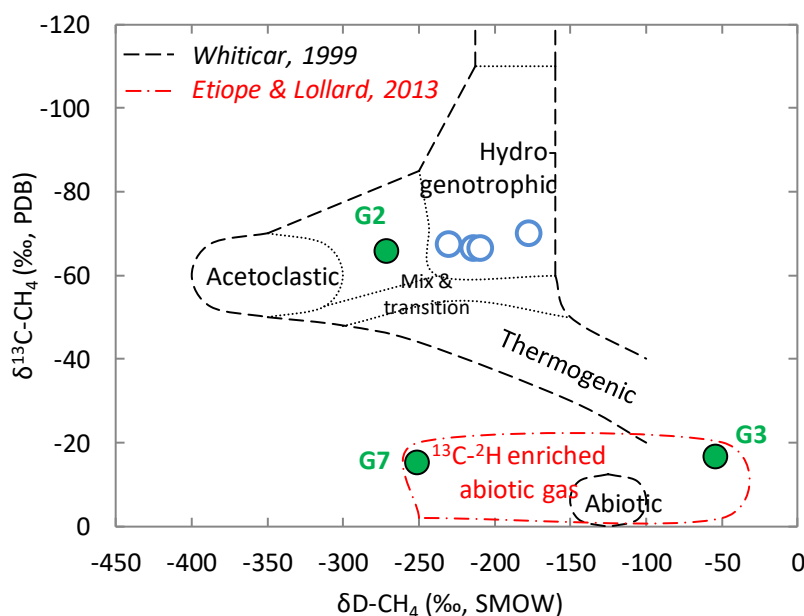


Figure 4. Carbon isotope composition ($\delta^{13}\text{C}$) as a function of hydrogen isotope composition ($\delta^2\text{H}$) for dissolved methane of pore waters (blue dots) and for methane of bubbling gases (green dots). The dotted black lines correspond to the range of $\delta^{13}\text{C}$ - $\delta^2\text{H}$ values defined by Whiticar⁷² for thermogenic

and bacterial methane (acetoclastic and hydrogenotrophic pathways). The red dotted line is the range of $\delta^{13}\text{C}$ - $\delta^2\text{H}$ values defined by Etiope and Lollar⁷³ for abiogenic methane.

Table 3. Chemical and isotope compositions of bubbling gases

Sample	CO ₂ (vol.%)	CH ₄ (vol.%)	O ₂ (vol.%)	N ₂ (vol.%)	$\delta^{13}\text{C}_{\text{CO}_2}$ (‰)	$\delta^{13}\text{C}_{\text{CH}_4}$ (‰)	$\delta\text{D}_{\text{CH}_4}$ (‰)
	±2% rel.	±2% rel.	±2% rel.	±2% rel.	±1‰	±1‰	±5‰
DZ16-08 G2	1.4	80.4	6.5	10.1	-20.1	-65.9	-272
DZ16-08 G3	95.5	0.6	2.6	2.7	-0.6	-16.8	-54
DZ16-08 G4	98.1	0.4	1.0	1.1	-0.3	-16.6	-
DZ16-08 G5	98.5	0.4	0.7	0.8	-2.0	-22.2	-
DZ16-08 G7*	99.2	0.3	0.2	0.6	-3.2	-15.4	-251
DZ16-08 G10	99.6	0.3	0.1	0.6	-2.4	-11.1	-
DZ16-08 G11	99.8	0.6	0.2	0.7	-2.2	-28.1	-
DZ16-08 G12	96.3	0.7	1.7	2.6	-1.4	-21.3	-

*Sample G7 is from the "Plage de l'aéroport" (airport beach), south of the volcanic crater.

±2% rel. indicates that the value is known with a precision of 2% relative to the measured value.

4.2 Radiocarbon measurements

Radiocarbon measurements of DIC and POC of the water column were performed to assess the lake reservoir effect, which can be large in volcanic crater lakes⁷⁴. DIC and POC have mean values of $\Delta^{14}\text{C}$ of $-566\pm3\text{‰}$ and $-554\pm2\text{‰}$, respectively (Table 4), which correspond to conventional radiocarbon ages of $6650\pm1\%$ years and $6420\pm1\%$ years. Given the half-life time of ^{14}C (5730 ± 40 years), those measurements indicate that DIC and POC contain between 55% and 60% of "dead" carbon (*i.e.*, non-atmospheric CO₂), evidencing the input of volcanic CO₂ into the lake and its contribution to autochthonous carbonate and organic matter production. Expectedly, the $\Delta^{14}\text{C}$ value of SIC and SOC in the surface sediment is close to that of DIC in the water column (except for one sample in the sediment core C2 (-87‰) composed primarily of terrestrial plant remains). Accordingly, plant macro-remains coming from the volcanic catchment rather than SIC and SOC were used to date the sediment. The radiocarbon data of macro-remains indicate ages of ca. 550 and 650 years at 45 cm and 79 cm, respectively (Table 5). The macro-remain recovered in the surface sediment (1 cm depth) has pre-Bomb values corresponding to 1955-1957 years AD (F^{14}C calibrated at 2σ with the program CALIBomb, Zone SH1-2⁷⁵).

364

Table 4. Radiocarbon data for water column and sediment

Sampling location ^a	Sampling date	Sample type	Sampling depth (cm)	age BP (year)	1 σ (year)	$\Delta^{14}\text{C}$ (‰)
DZ11-9 WC	Sept. 2011	DIC	10	6700	35	-569
DZ12-4 WC	April 2012	DIC	10	6590	30	-563
DZ10-9 WC	Sept. 2010	POC	50	6460	35	-556
DZ10-9 WC	Sept. 2010	POC	300	6375	35	-551
DZ12-4 C1	April 2012	SIC	2.5-5.0*	6460	30	-556
DZ12-4 C1	April 2012	SIC	11-16*	5515	30	-500
DZ12-4 C1	April 2012	SOC	5.0-7.5*	5720	30	-513
DZ12-4 C1	April 2012	SOC	11-16*	4875	30	-459
DZ12-4 C1	April 2012	SOC	11-16*	4415**	30	-427
DZ12-4 C1	April 2012	SOC	22-30*	5730**	30	-514
DZ12-4 C1	April 2012	SOC	37-40*	6045**	35	-532
DZ12-4 C2	April 2012	SIC	0-2.5*	6545	30	-561
DZ12-4 C2	April 2012	SIC	10.5-14.0*	6205	30	-542
DZ12-4 C2	April 2012	SOC	2.5-4.5*	5450	30	-496
DZ12-4 C2	April 2012	SOC	10.5-14.0*	675	30	-87
DZ12-4 C2	April 2012	SOC	27-30*	5600	35	-506

^aWC is for water column, C1 and C2 for the sediment core 1 and 2

*depth of the sediment layer; ** additional acid pre-treatment with 1M HCl solution at room temperature

365

366

Table 5. Radiocarbon dating of terrestrial plant macro-remains of the sediment core C12

Depth (cm)	¹⁴ C age BP	Err 1 σ	F ¹⁴ C	Err 1 σ	Burial rate (mm·yr ⁻¹)
1	-	-	1.0161	0.0084	
	-	-	1.0135	0.0084	
45	582	71	0.9301	0.0078	0.77
	508	69	0.9387	0.0077	0.89
79	666	68	0.9204	0.0078	1.19
	653	63	0.9219	0.0072	1.21

367 Two measurements per sample.

368

369 4.3 Porosity and sedimentation rate

370 The porosity decreases from 98% in the surface sediment to 80-85% at depth (Fig. 5, Table S5 in
 371 supporting information). The best fit of the porosity profile ($r^2=0.6$) can be expressed as a log
 372 distribution because of the large porosity changes in the upper centimeters:

$$373 \quad \phi(z) = -0.0199 \cdot \ln(z) + 0.881 \quad \text{Eqs (6)}$$

374 where ϕ is the porosity and z is the depth in meter. The correlation coefficient is explained by the
 375 spread of the porosity values at depth. Equation 6 is consistent with the mean porosity values all along
 376 the sedimentary column.

377 Radiocarbon measurements of plant macro-remains in the sediment enabled to determine ages as
 378 function of depth (Table 5). This approach is reasonable as no textural evidence has been observed on
 379 the first meter of sediment that could indicate erosion episodes or changes in the depositional

environment³³. The age-depth model allowed estimating an asymptotic burial rate at 5 m depth of 0.75 mm·yr⁻¹. Then, the asymptotic burial rate and the porosity profile were used solved the equations (3) and (4). The solid burial rate decreases from 5 mm·yr⁻¹ in the uppermost sediment to 1 mm·yr⁻¹ at 1 m depth (Fig. 5).

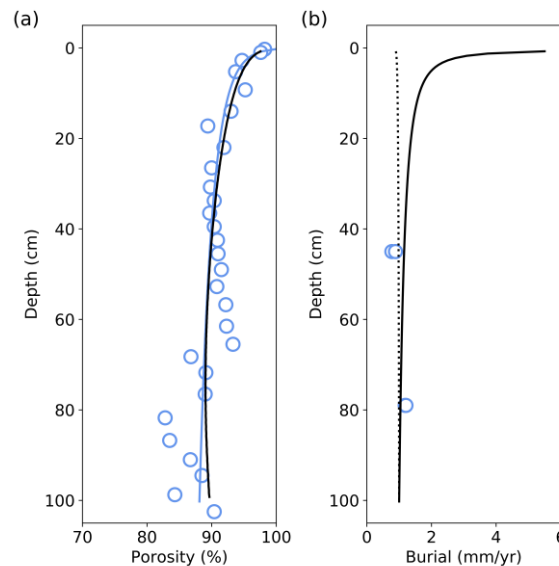
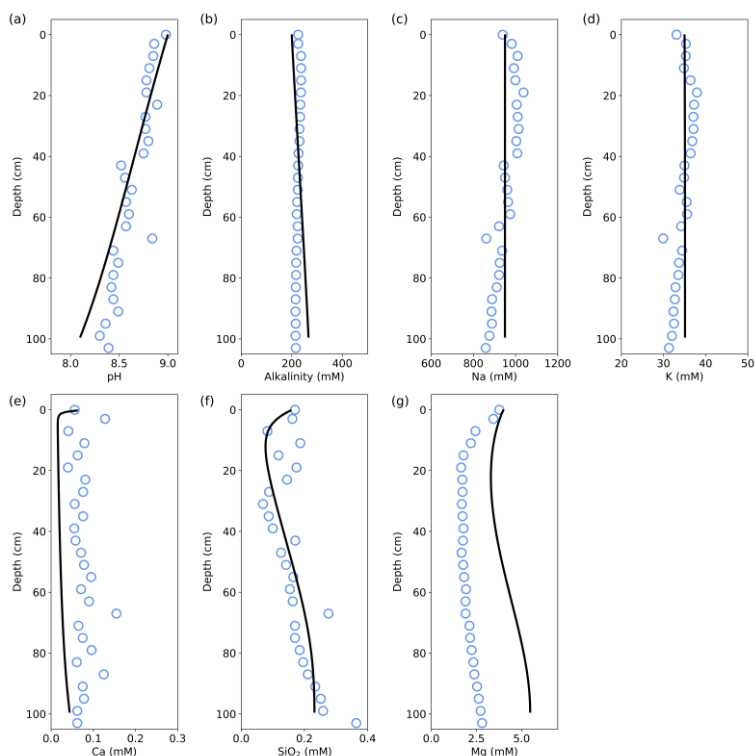


Figure 5. Measured and modeled porosity profiles (a) and calculated profiles for fluid and solid burial rates (b) as a function of depth. (a) Measured porosity (blue circles), and modeled porosity profile (black thick line). The blue line is a fit of the porosity data used for the burial rate calculation (Eqs 6; $r^2=0.6$). (b) Fluid and solid burial rates (mm·yr⁻¹) used in the model. The depth-age constraints used for the burial rate calculation are shown with open blue circles and are obtained from the radiocarbon dating of plant macro-remains.

4.4 Chemical composition of pore waters

The pH values of pore waters decrease from 9 near the water-sediment interface to 8.3 at 1 m depth (Fig. 6, Table S6 in supporting information). The alkalinity and the concentrations of sodium and potassium are of 235 mM, 1000 mM and 37 mM, respectively, in the surface sediment and decrease slightly at depth. The calcium concentration remains constant at ca. 75 μ M, while the silicon concentration increases from 150 μ M at the sediment surface to 250 μ M at 1 m depth. The magnesium concentration decreases down to 2 mM near the water-sediment interface and then increases slowly below 20 cm depth.



5. Figure 6. Comparison of measured and modeled pH values, alkalinity and major cations concentrations in the pore waters. The blue dots and the full black lines represent the measured and modeled values, respectively. Model results are after 4000 years of calculation. Modeling and discussion

5.1 Carbon cycle and controls on pH

The Dziani Dzaha is characterized by an unusual carbon cycle, for which the main characteristics are caught in Figure 7. Both CO₂ and methane are outgassing from the lake water to the atmosphere. The carbon and hydrogen isotope signatures of dissolved methane of sediment pore waters are typical of bacterial methanogenesis through the hydrogenotrophic pathway⁷². The intense bacterial methanogenesis in the sediment and in the lake water³⁹ results in saturated concentrations of methane in the lake water column and in CH₄-dominated bubbling gases (Sample G2). The formation of CH₄ during hydrogenotrophic methanogenesis can be written as:



The microbial fermentation of the organic matter is the most likely source of CO₂ and H₂ and could also account for the decrease of pore water pH values with depth. The coupled mechanisms of methanogenesis and fermentation can be represented by the simplified reaction:



with CH₂O being a simplified stoichiometry for the organic matter.

Magmatic CO₂ inputs is also likely influencing the pH of pore waters. The CO₂-dominated gases bubbling into the lake evidence an active magmatic degassing. The δ¹³C and δ²H values of CH₄ in samples G3, G4, G10 and G7 are consistent with an abiotic origin⁷³. The lower δ¹³C-CH₄ values of G5, G11, G12 and G2 reflect mixing between abiotic and microbial methane during the ascent of the bubbling gases through the water column, with an overwhelming dominance of microbial methane for G2, possibly due to the higher height of the water column where G2 was sampled. The chemical and isotopic compositions of CO₂-dominated bubbling gases are consistent with a magmatic origin.

The radiocarbon measurements of inorganic and organic carbon of the water column indicate that the magmatic CO₂ contributes to the carbonate and organic matter production by more than 50 mol.%. This additional source of carbon fuels the massive primary productivity of the lake dominated by cyanobacteria³⁹. In turn, the photosynthetic activity of the cyanobacteria is the most likely processes at the origin of the overall high pH values, according to the reaction:

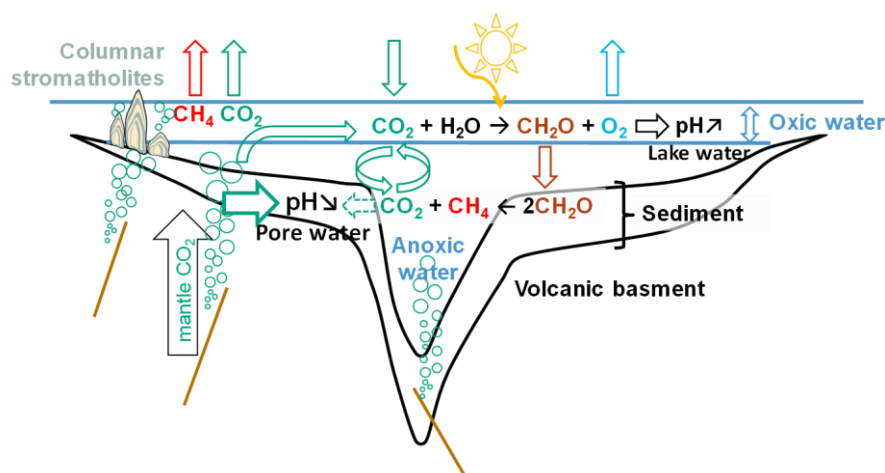


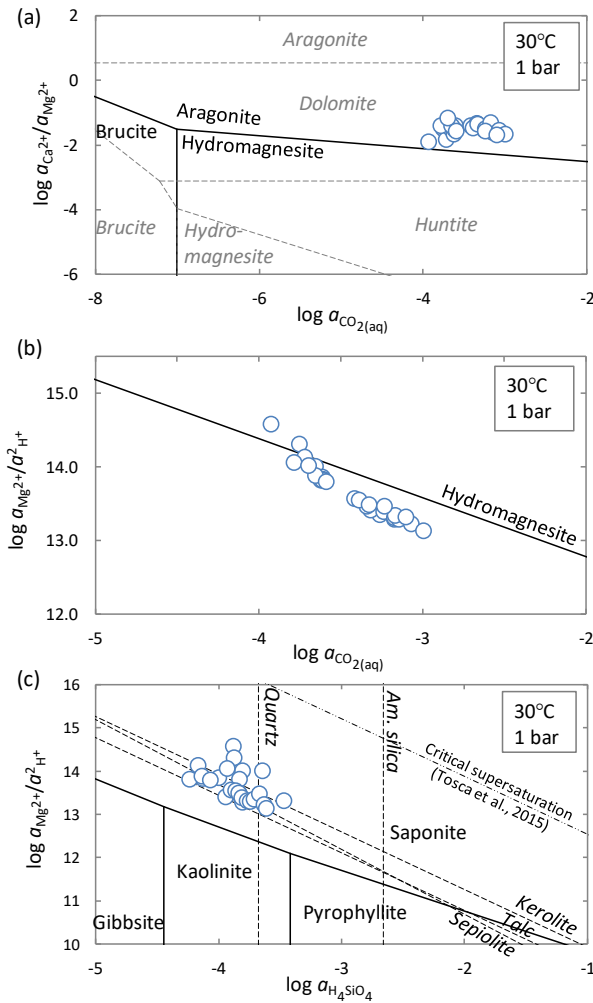
Figure 7. Schematic diagram of the carbon cycle and its controls on both lake water and pore waters pH values. Photosynthetic organisms in shallow waters use CO₂ originating from the atmosphere, from the magmatic gases CO₂ inputs and from organic matter degradation. The photosynthetic activity results in a production of O₂ which is lost to the atmosphere, in an increase of the lake water pH, and in organic matter accumulating in the sediment. In the water column and the sediment, the microbial degradation of the organic matter produces CH₄ and CO₂ which, associated to the magmatic CO₂ inputs, induce a decrease of the pore water pH values. Both CO₂ and biogenic CH₄ escape to the atmosphere. The size of the arrows pointing toward the pH decrease of pore waters

illustrates the dominant contribution of the magmatic CO₂ and the lower impact of the organic matter microbial degradation.

5.2 Mineral stability

The metastable equilibria between aragonite, hydromagnesite and brucite were calculated as a function of Mg²⁺, Ca²⁺ and CO₂ activities (Fig. 8a). Although thermodynamics suggests that magnesite and dolomite are the most stable Mg-bearing carbonates at surface temperature and pressure, kinetics exerts a strong primary control on their formation^{67,77,78}. The pore waters are close to metastable equilibrium between aragonite and hydromagnesite, which is consistent with the presence of the two carbonates in the surface sediment. While the Ca²⁺/Mg²⁺ ratio is relatively stable with depth, the decrease of pH induces an increase of the CO₂ activity, which promotes the stability of aragonite at the expense of hydromagnesite. Dolomite has been locally observed at depth in the sediment³³ and could form by Mg incorporation and Ca replacement in calcium carbonates^{78,79}. The progressive hydromagnesite undersaturation with depth stems from the pH decrease in pore waters (Fig. 8b).

The stability domains of Mg-aluminosilicates and those of talc, kerolite and sepiolite are calculated as function of H⁺, Mg²⁺ and SiO₂ activities considering that aluminum behaves conservatively between the Al-bearing minerals (Fig. 8c). Chlorites are not considered as their formations are kinetically limited at ambient temperature and pressure⁸⁰. The pore waters are supersaturated relative to saponite and remain supersaturated at depth despite the pH decrease. The Mg-aluminosilicate likely forms through heterogeneous nucleation involving mineral precursors such as alkaline feldspars, which lower the supersaturation required for mineral nucleation⁸¹. The Al-free Mg-silicates, although stable in the pore waters, are not observed in the sediments. Tosca⁸¹ proposed a critical supersaturation above which those Mg-silicates would precipitate through homogeneous nucleation. The precipitation of hydromagnesite and saponite, by removing magnesium and silica from the pore waters, likely hinder the formation of Al-free Mg-silicates.

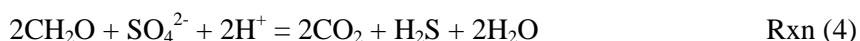


469

470 Figure 8. Pore water compositions (blue circles) and mineral stability domains in the systems (a) Mg-
 471 Ca-C-O-H, (b) Mg-C-O-H and (c) Mg-Al-Si-O-H at 30°C and 0.1 MPa. Mineral stability domains
 472 were calculated with the Thermoddem database^{13,14} and pore waters were speciated with the Phreeqc
 473 software⁸². (a) Magnesite and calcite are not considered in the calculation as they are not present in the
 474 sediment. The grey dotted lines are metastable equilibria between dolomite, huntite, aragonite,
 475 hydromagnesite and brucite. The full lines are metastable equilibria between aragonite,
 476 hydromagnesite and brucite. (b) The full line corresponds to fluid composition at equilibrium with
 477 hydromagnesite. (c) The full lines are metastable equilibria between Mg-aluminosilicates without
 478 considering chlorites. The dotted lines are fluid compositions at equilibrium with talc, sepiolite and
 479 kerolite. Thermodynamic data for kerolite are from Stoessel⁸³. The dashed-dotted line is the critical
 480 supersaturation required for homogenous nucleation of Mg-silicates as suggested by Tosca⁸¹. Silica
 481 activities at equilibrium with quartz and amorphous silica are shown for reference (vertical dotted
 482 lines).

5.3 Reactive transport modeling

The model is based on the sediment composition of the core C4, which was collected approximately at the average lake water depth (Fig. 1) and has a composition well representative of the dominant sediment composition observed in most sediment cores³³. The mineral and pore water compositions are constant from 1500 years to 4000 years (end of the simulation), showing that a steady state has been reached. The microbial degradation of organic matter according to Reaction (2) results in a decrease of its content with depth and a decrease of pH through the release of CO₂. The rate constant of the organic matter degradation is adjusted to best fit the profile of organic matter content. A value of $10^{-10.3} \text{ mol} \cdot \text{m}^{-2} \cdot \text{s}^{-1}$ is adopted (Table 1), close to published values⁵⁴. The modeled concentration of methane in the uppermost part of the sediment column is consistent with the dissolved methane measured in the lake water column at the corresponding depth (i.e., 3-4 m of water height) (Fig. 3), which supports the use of methanogenesis and fermentation to approximate the overall organic matter degradation. If no external source of CO₂ is considered, the modeled pH value at 1 m depth is 0.7 pH units higher than the measured value and the total CO₂ pressure is of $6.3 \cdot 10^{-3}$ bar. In our model, CO₂ is thus injected at the bottom of the sediment column to account for the influence of magmatic CO₂. The best fit of pH is obtained with a CO₂ injection of $4 \text{ mmol} \cdot \text{s}^{-1} \cdot \text{m}^{-3}$ of sediment, which results in a total CO₂ pressure of $7.5 \cdot 10^{-2}$ bar at 1 m depth, one order of magnitude higher than without CO₂ injection (Fig. 6). The corresponding CO₂ concentration is of 2 mM, which does not exceed the CO₂ solubility of the lake (16 mM) and is consistent with the absence of bubbling CO₂ where the sediment core C4 was collected. At 1 m depth, our model predicts magmatic CO₂ inflows and organic matter degradation accounting for 22 and 2 mol.% of the pore water DIC, respectively. The remaining DIC is inherited from the lake water by diffusion and fluid burial. The sulfur cycle, not considered in the model, is not expected to modify significantly these results. The sulfate concentrations of ca. 2 mM in the lake water³⁹ indicate a low contribution of sulfate to the alkalinity compared to bicarbonate ions. Sulfate reduction coupled to organic matter oxidation would produce twice as many times CO₂ per mole of reaction as the organic matter degradation considered in the model (Reaction 2) according to:



The low sulfate concentration does not seem compatible with high densities of sulfate-reducing bacteria outcompeting methanogens³⁹; however, even in the unlikely case where all organic matter degradation results from sulfate reduction, the process would only account, in first approximation, for ca. 4 mol.% of the total pore water DIC which remains a minor contribution compared to the magmatic CO₂ inflows.

The modeled alkalinity and major cation profiles are consistent with the measured data (Fig. 6). Magnesium shows a distinctive concentration profile compared to the other dissolved species, with a decrease in concentration in the surface sediment followed by a moderate increase at depth. Despite a shift toward higher values, the modeled profile is consistent with the measurements. Hydromagnesite exerts a strong control on the dissolved Mg. Its precipitation in the shallow sediment lowers the Mg concentrations, which increase at further depth where hydromagnesite is destabilized. A decrease of the CO₂ inflows at the bottom of the sediment column allows a better fit of the Mg profile; however, the pH values become higher than the measured ones and the hydromagnesite is less destabilized at depth. When CO₂ inflows are suppressed, the pH does not decrease enough to destabilize the hydromagnesite. A decrease of the hydromagnesite solubility decreases the Mg concentration but increases the Mg-carbonate content at depth. The discrepancy between the measured and modeled Mg profile could be explained by the precipitation of amorphous Mg-Si phases as precursors of Mg-phylosilicates⁸¹, which are not considered in our model. The silica concentration is controlled by the formation of saponite and microcline. If saponite or microcline are suppressed from the model, the silica concentration increases to value up to one order of magnitude higher than the measured ones, showing the role of these phases in the silica balance of the lake. The formation of microcline is consistent with evidences of low-temperature K-feldspars authigenesis in natural environments^{84,85}. Equilibrium of the pore waters with amorphous Mg-Si phases⁶⁴, not considered in the model, could also contribute to the buffering of the silica concentration. A reasonable consistency is obtained between the modeled and measured calcium concentrations. The underestimation of the Ca concentrations can result from an aragonite solubility higher in the Dziani Dzaha than reported in the Thermoddem database. An increase by 0.5 of the logarithmic value of the aragonite equilibrium constant shifts the modeled calcium concentrations toward values consistent with the measured ones.

The modeled sediment composition is also consistent with the observations (Fig. 9). The solid phase of surface sediment is dominated by organic matter and aragonite, with lower amounts of detrital silicates and saponite. The hydromagnesite content represents 17 wt.% of the solid phase at 60 cm and decreases at further depth. The organic matter content decreases from 42 wt.% of the solid phase in the uppermost sediment to 23 wt.% at depth due to microbial degradation. The decrease of pH down to 8.2 at 1 m depth induces the destabilization of hydromagnesite, which matches the observations although the model overestimates the hydromagnesite content. An increase of the CO₂ inflows decreases the hydromagnesite content at depth, which is more consistent with the observations; however, the pH values and the Mg concentrations become under and overestimated, respectively. Aragonite and saponite remain stable despite the pH decrease and saponite accumulates at depth to reach 17 wt.% of the solid phase. The destabilization of hydromagnesite in parallel to the formation of saponite could evidence a reaction relationship between the two minerals³³; however, suppressing the hydromagnesite of the model leads to similar yield of saponite, showing that the

magnesium required for the saponite formation is primarily supplied by the lake water. An increase of the precipitation rate of saponite does not lead to a significant increase of the saponite content; however, it results in a drastic decrease of the aluminium concentration from 10^{-4} μM to 10^{-6} μM , which highlights aluminium as the limiting reactant in the saponite formation. As consequence, the pore waters become undersaturated relative to the K-feldspar due to the aluminium decrease. Microcline does not form anymore, and the silica concentrations increase above measured values. The diopside content decreases with depth as the mineral dissolves; however, a specific surface area one order of magnitude higher than the literature values is used to achieve this result (Table 1). Alternatively, higher inputs of detrital materials to the lake in recent times could explain the observed increase of the diopside content in the uppermost sediment. Quartz and dolomite do not form due to kinetic limitations and the pore waters are undersaturated relative to gibbsite.

The role of the sediment compaction was tested running the model considering a same burial rate for fluid and solid phases. The results are very similar, which shows that the sediment compaction has low influence on the temporal and spatial time scale of the Dziani Dzaha early diagenetic processes. Additional sensitivity tests were performed to validated the robustness of the model (supporting information).

In summary, the model allowed to discriminate and quantify the role of magmatic CO_2 inflows and organic matter microbial degradation on the diagenetic evolution of the sediment. Without magmatic CO_2 inflows, the decrease of pH and the destabilization of hydromagnesite at depth cannot be explained. The magmatic CO_2 inputs oversees 90% of the pH decrease of the pore waters. The organic matter degradation accounts for the remaining 10% while the only mineral reactivity has no significant impact on pH. The model allowed quantifying the flux of magmatic CO_2 ($4 \text{ mmol}\cdot\text{s}^{-1}\cdot\text{m}^{-3}$) and the fraction of the lake DIC inherited from the magmatic gases (22 mol.%). The model also highlights the lake water as the primary source of Mg, aluminum as the limiting reactant in the saponite formation and the K-feldspar controlling the Si concentrations. Isotopes composition, not treated in the model, could bring additional constrain on rate and processes^{10,17,86}. Future modeling efforts will have to integrate isotopic data to fully decipher the early diagenesis of the Dziani Dzaha sediment.

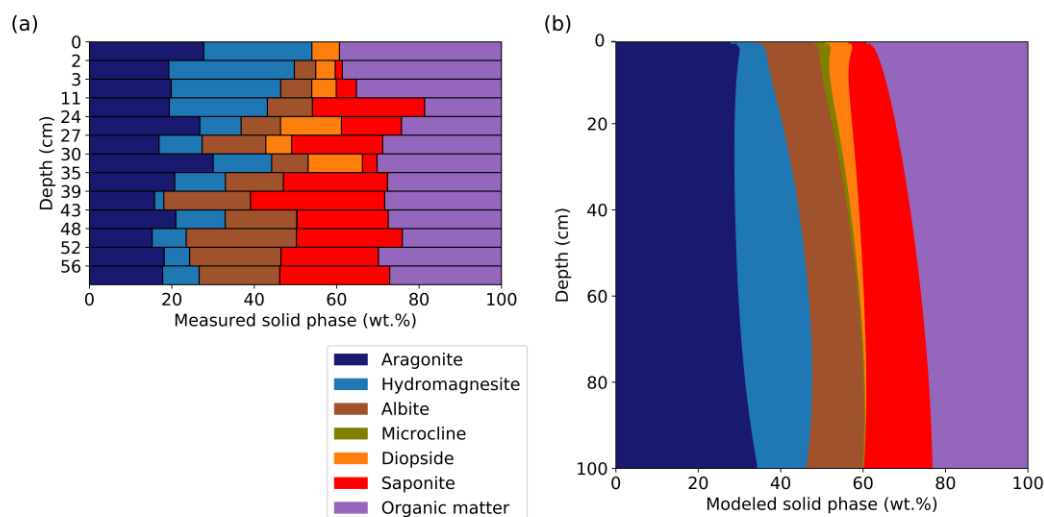


Figure 9. Observed and modeled sediment composition (wt.%) as a function of depth. (a) Measured composition in the sediment core C4³³. (b) Modeled sediment composition. Dark blue, light blue, brown, green, orange, red and purple are for aragonite, hydromagnesite, albite, microcline, diopside, saponite and organic matter, respectively. Model results are after 4000 years of calculation.

5.4 Insights on the formation of lacustrine carbonates in volcanic-dominated settings

These data provide new insights on the origin of carbonates and Mg-silicates produced in lacustrine environments in volcanic-dominated settings such as continental rifts^{6-8,87}. Mg-silicates (stevensite, kerolite and talc) have been identified in the Cretaceous pre-salt carbonate rocks of the South Atlantic continental margins²⁷. Their formation was suggested to occur in lakes dominated by volcanic terrains^{8,88}, but it is unclear whether it is a sufficient source of silica and magnesium to fuel the Mg-silicates precipitation. Experimental work by Tutolo and Tosca³⁰ showed that, at elevated pH and Si concentration, the precipitation of Mg-silicates and spheroidal calcium carbonates typical of the pre-salt formation requires moderate Ca and Mg concentrations, $< 1-2 \text{ mmol} \cdot \text{kg}^{-1}$. This implies high fluxes of Ca and Mg to the site of deposition to explain the volume of the carbonate rocks. Our study shows that the weathering of alkaline volcanic rocks in a small-scale basin can be enough to supply the Ca, Mg and Si needed for carbonates and Mg-silicates to form. The formation of Mg-silicates and K-feldspars would buffer the silica concentration. Alkaline volcanic terrains can also supply enough aluminium for saponite to form. Aluminium being shown as the limiting reactant in the saponite formation, the occurrence of Mg-aluminosilicates sets paleoenvironmental constraints on the nature of the volcanic terrains required for their formation.

The origin of the high pH values required for the formation of Mg-silicates remains unclear. Specific geochemical conditions are required to produce high pH waters in evaporating lake³⁰.

Depending on the ratio between Ca concentration and alkalinity, the formation of carbonates can prevent the pH to reach values high enough for Mg-silicates to form. An intense primary productivity, as identified in the Dziani Dzaha, can make the difference by pushing the pH to those high values. This intense primary productivity is probably due to the combination of nutrient input by the weathering of alkaline volcanic rocks and the lake functioning, ammonium and phosphate generated by the organic matter degradation in the anoxic part of the water column being recycled for primary productivity rather than denitrified (for ammonium) or buried in the sediment together with iron oxides.

The initial mineralogy of the carbonate rocks of the South Atlantic margins is still unknown. High contents of Sr measured in spherulitic calcite of the pre-salt deposits of the Angolan margin could support an aragonitic component of initial mineralogy²⁸. Precipitation of aragonite rather than calcite is dependent on the Mg/Ca ratio, for which values above 10 tend to promote the formation of aragonite at the expense of calcite⁸⁹⁻⁹¹. Delay between carbonates and Mg-silicates formation during early diagenesis tends to increase the Mg/Ca ratio favoring the formation of aragonite³⁰. The Mg/Ca ratio of ca. 20 of the Dziani Dzaha lake and pore waters is consistent with the occurrence of aragonite. Our field and model results highlight the differing time scales of carbonates and Mg-silicates formation during the early diagenesis, with saponite accumulating mostly at depth whereas aragonite is present in the surface sediment. The Dziani Dzaha is a good example of geochemical environments co-precipitating carbonates and Mg-silicates and promoting the formation of aragonite at the expense of calcite. Moreover, the Mg concentration of the Dziani Dzaha pore waters is shown to be controlled by the precipitation and destabilization of hydromagnesite, which can thus influence both the formation of Mg-silicates and the nature of the Ca-carbonates. The formation of hydromagnesite in the surface sediment can hinder the formation of Mg-silicates whereas its destabilization at depth can fuel the Mg-silicates formation and increase the Mg/Ca ratio, stabilizing the aragonite.

The volume and spatial extent of the continental carbonate rocks deposited in the South Atlantic continental rift at a time of isolation from the ocean (Early Cretaceous, 142-113Ma)^{28,29,92} raise questions about the carbon source. During continental rifting, magmatic CO₂ inflows could have occurred as the continental crust became thinner and the influence of asthenospheric mantle increased. Our study demonstrates the ability of magmatic CO₂ inflows to fuel the carbonate production into small-scale basin. By analogy, CO₂ inflows may have set the appropriate geochemical conditions for the pre-salt Mg-silicate-rich carbonates to form by fueling the carbonate factory and the primary productivity, which in turn resulted in high pHs promoting the Mg-silicates formation.

The occurrence of pore-filling Mg-silicates in carbonate reservoir rocks is expected to lower the reservoir quality by decreasing porosity and permeability. However, the diagenetic processes which may affect the stability of these chemically labile minerals are not well understood. Although

the pore waters remain supersaturated relative to saponite all along the first meter of the Dziani Dzaha sediment, the decrease of pH induces a progressive decrease of the saponite supersaturation. In a context of continental rifting under magmatic CO₂ influence, a further decrease of pH at depth could eventually destabilize the Mg-silicates and increase the porosity. Investigating the fate of saponite at further depth in the Dziani Dzaha sediment would provide new insights on the stability of these labile minerals during diagenesis.

This study did not account for the iron and sulfur cycle. Considering the iron cycle is an unavoidable step towards the understanding of geological units such as pre-salt sedimentary sequences in which iron bearing phases such as titanomagnetite and siderite were identified in the paragenetic sequence⁹³. Further characterization efforts will have to focus on the iron and sulfur sources and sinks to fully investigate diagenetic evolution of the Dziani Dzaha sedimentary sequences.

6. Concluding remarks

A detailed characterization of the Dziani Dzaha sediments was performed and used to develop a reactive-transport model accounting for burial rate and sediment compaction. The model allowed to discriminate and quantify the role of magmatic CO₂ inflows and organic matter microbial degradation on the diagenetic evolution of the sediment. While our ¹⁴C radiometric data show that the magmatic CO₂ fuels both the primary productivity and the carbonate formation, the model indicates that it is also responsible of the decrease of the pore water pHs from 9 to 8.2 in the first-meter of sediment. As consequence, the hydromagnesite is destabilized at depth leaving behind an aragonite - saponite mineral assemblage. Saponite formation is shown to be limited by aluminium availability, which brings constrain on the paleoenvironments of formation of Mg-aluminosilicates. These results bring new insight on the formation and diagenesis of carbonate sediments associated with Mg-silicates in volcanic-dominated settings such as continental rifting. They demonstrate the possible role of magmatic CO₂ in setting the geochemical conditions required for the co-precipitation of carbonate and Mg-silicates, by supplying carbon to the carbonate factory, by fueling the primary production which in turn raises the pHs and enhances the carbonate and Mg-silicates formation, and by controlling the pore water pHs during diagenesis. The ability of our model to reproduce the porosity, the pore water chemistry and the mineral assemblage of the Dziani Dzaha sediments makes it very promising to predict the full evolution of chemical and physical properties of larger-scale carbonate formation from their deposition to their current settings.

672 This work was supported by IPGP, TOTAL (project FR00008189), Agence Nationale de la Recherche
673 (France) (grant number ANR-13-BS06-0001) and one INSU-INTERRVIE grant (grant number
674 AO2013-785992). Radiocarbon analysis benefited from funding by INSU-CNRS (ARTEMIS 2014)
675 and the Deep Carbon Observatory and analytical support by J.P. Dumoulin and C. Moreau, LMC14.
676 The funding for Carl Steefel was provided by the Director, Office of Science, Basic Energy Sciences,
677 Chemical Sciences, Geosciences, and Biosciences Division, of the U.S. Department of Energy under
678 Contract No. DE-AC02-05CH11231 to Lawrence Berkeley National Laboratory. The authors also
679 wish to thank their colleagues (C. Leboulanger, C. Bernard, P. Got, E. Fouilland, M. Bouvy, E. Le
680 Floch, V. Grossi and D. Sala) for their support and assistance during sampling campaigns on Dziani
681 Dzaha. Hélène Vermesse and Sonia Noirez are acknowledged for their assistance during molecular
682 and isotopic analyses of gases at IFPEN. Finally, the authors thank the Air Austral Airline Company
683 and Alexandra and Laurent at the “Les Couleurs” Guest House in Mayotte for their valuable assistance
684 and support.

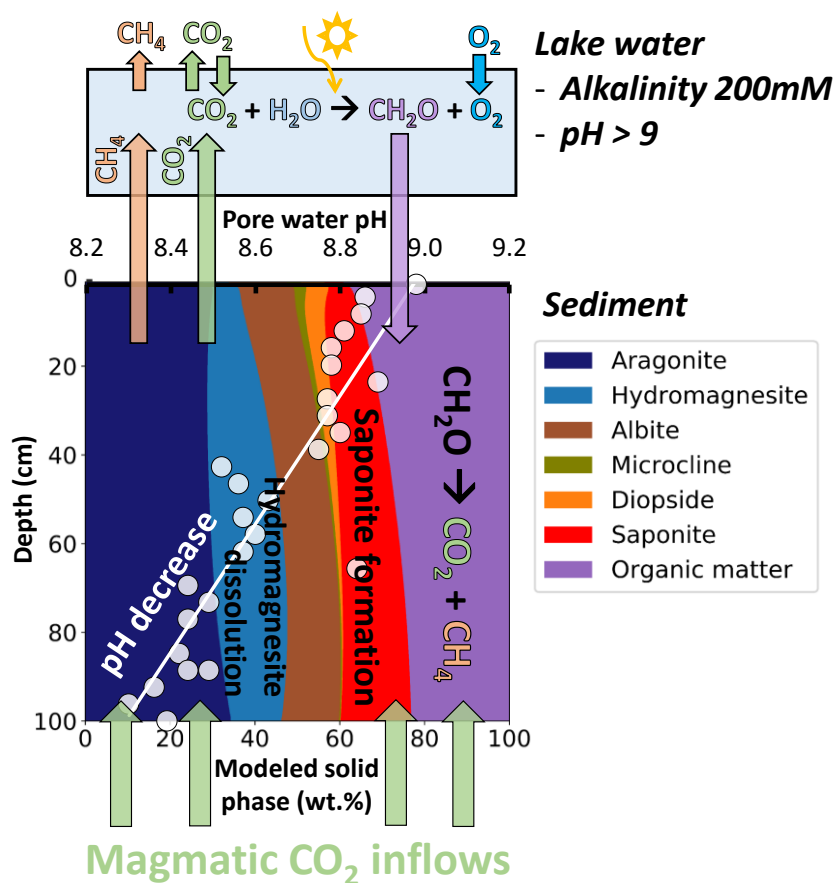
- 686 (1) Back, W.; Hanshaw, B. B.; Plummer, L. N.; Rahn, P. H.; Rightmire, C. T.; Rubin, M. Process and Rate
687 of Dedolomitization: Mass Transfer and ¹⁴C Dating in a Regional Carbonate Aquifer. *GSA Bulletin*
688 **1983**, 94 (12), 1415–1429. [https://doi.org/10.1130/0016-7606\(1983\)94<1415:PARODM>2.0.CO;2](https://doi.org/10.1130/0016-7606(1983)94<1415:PARODM>2.0.CO;2).
- 689 (2) Machel, H. G. Concepts and Models of Dolomitization: A Critical Reappraisal. *Geological Society,*
690 *London, Special Publications* **2004**, 235 (1), 7–63. <https://doi.org/10.1144/GSL.SP.2004.235.01.02>.
- 691 (3) Morad, S. *Carbonate Cementation in Sandstones: Distribution Patterns and Geochemical Evolution*;
692 John Wiley & Sons, 2009; Vol. 72.
- 693 (4) Hill, C. A. Sulfuric Acid Speleogenesis of Carlsbad Cavern and Its Relationship to Hydrocarbons,
694 Delaware Basin, New Mexico and Texas (1). *AAPG bulletin* **1990**, 74 (11), 1685–1694.
- 695 (5) Hill, C. A. H₂S-Related Porosity and Sulfuric Acid Oil-Field Karst. **1995**.
- 696 (6) Bertani, R. T.; Carozzi, A. V. Lagoa Feia Formation (Lower Cretaceous) Campos Basin, Offshore Brazil:
697 Rift Valley Type Lacustrine Carbonate Reservoirs - I. *J Petroleum Geol* **1985**, 8 (1), 37–58.
698 <https://doi.org/10.1111/j.1747-5457.1985.tb00190.x>.
- 699 (7) Bertani, R. T.; Carozzi, A. V. Lagoa Feia Formation (Lower Cretaceous) Campos Basin, Offshore Brazil:
700 Rift Valley Type Lacustrine Carbonate Reservoirs - II. *Journal of Petroleum Geology* **1985**, 8 (2), 199–
701 220. <https://doi.org/10.1111/j.1747-5457.1985.tb01011.x>.
- 702 (8) Wright, V. P. Lacustrine Carbonates in Rift Settings: The Interaction of Volcanic and Microbial
703 Processes on Carbonate Deposition. *Geological Society, London, Special Publications* **2012**, 370 (1), 39–
704 47. <https://doi.org/10.1144/SP370.2>.
- 705 (9) Machel, H. G. Bacterial and Thermochemical Sulfate Reduction in Diagenetic Settings — Old and New
706 Insights. *Sedimentary Geology* **2001**, 140 (1–2), 143–175. [https://doi.org/10.1016/S0037-0738\(00\)00176-7](https://doi.org/10.1016/S0037-0738(00)00176-7).
- 707 (10) Ahm, A.-S. C.; Bjerrum, C. J.; Blättler, C. L.; Swart, P. K.; Higgins, J. A. Quantifying Early Marine
708 Diagenesis in Shallow-Water Carbonate Sediments. *Geochimica et Cosmochimica Acta* **2018**, 236, 140–
709 159. <https://doi.org/10.1016/j.gca.2018.02.042>.
- 710 (11) Berner, R. A. *Early Diagenesis: A Theoretical Approach*; Princeton University Press, 1980.
- 711 (12) Li, L.; Maher, K.; Navarre-Sitchler, A.; Druhan, J.; Meile, C.; Lawrence, C.; Moore, J.; Perdril, J.;
712 Sullivan, P.; Thompson, A.; et al. Expanding the Role of Reactive Transport Models in Critical Zone
713 Processes. *Earth-Science Reviews* **2017**, 165, 280–301. <https://doi.org/10.1016/j.earscirev.2016.09.001>.
- 714 (13) Blanc, Ph.; Lassin, A.; Piantone, P.; Azaroual, M.; Jacquemet, N.; Fabbri, A.; Gaucher, E. C.
715 Thermodem: A Geochemical Database Focused on Low Temperature Water/Rock Interactions and
716 Waste Materials. *Applied Geochemistry* **2012**, 27 (10), 2107–2116.
717 <https://doi.org/10.1016/j.apgeochem.2012.06.002>.
- 718 (14) Blanc, P.; Vieillard, P.; Gailhanou, H.; Gaboreau, S.; Gaucher, E.; Fialips, C. I.; Made, B.; Giffaut, E. A
719 Generalized Model for Predicting the Thermodynamic Properties of Clay Minerals. *American Journal of*
720 *Science* **2015**, 315 (8), 734–780. <https://doi.org/10.2475/08.2015.02>.
- 721 (15) Marty, N. C. M.; Claret, F.; Lassin, A.; Tremosa, J.; Blanc, P.; Madé, B.; Giffaut, E.; Cochepin, B.;
722 Tournassat, C. A Database of Dissolution and Precipitation Rates for Clay-Rocks Minerals. *Applied*
723 *Geochemistry* **2015**, 55, 108–118. <https://doi.org/10.1016/j.apgeochem.2014.10.012>.
- 724 (16) Marty, N. C. M.; Lach, A.; Lerouge, C.; Grangeon, S.; Claret, F.; Fauchet, C.; Madé, B.; Lundy, M.;
725 Lagroix, F.; Tournassat, C.; et al. Weathering of an Argillaceous Rock in the Presence of Atmospheric
726 Conditions: A Flow-through Experiment and Modelling Study. *Applied Geochemistry* **2018**, 96, 252–
727 263. <https://doi.org/10.1016/j.apgeochem.2018.07.005>.
- 728 (17) Maher, K.; Steefel, C. I.; DePaolo, D. J.; Viani, B. E. The Mineral Dissolution Rate Conundrum: Insights
729 from Reactive Transport Modeling of U Isotopes and Pore Fluid Chemistry in Marine Sediments.
730 *Geochimica et Cosmochimica Acta* **2006**, 70 (2), 337–363. <https://doi.org/10.1016/j.gca.2005.09.001>.
- 731 (18) Arndt, S.; Jørgensen, B. B.; LaRowe, D. E.; Middelburg, J. J.; Pancost, R. D.; Regnier, P. Quantifying
732 the Degradation of Organic Matter in Marine Sediments: A Review and Synthesis. *Earth-Science*
733 *Reviews* **2013**, 123, 53–86. <https://doi.org/10.1016/j.earscirev.2013.02.008>.
- 734 (19) Paraska, D. W.; Hipsey, M. R.; Salmon, S. U. Sediment Diagenesis Models: Review of Approaches,
735 Challenges and Opportunities. *Environmental Modelling & Software* **2014**, 61, 297–325.
736 <https://doi.org/10.1016/j.envsoft.2014.05.011>.
- 737 (20) Huber, C.; Druhan, J. L.; Fantle, M. S. Perspectives on Geochemical Proxies: The Impact of Model and
738 Parameter Selection on the Quantification of Carbonate Recrystallization Rates. *Geochimica et*
739 *Cosmochimica Acta* **2017**, 217, 171–192. <https://doi.org/10.1016/j.gca.2017.08.023>.
- 740 (21) Hayes, J. M.; Waldbauer, J. R. The Carbon Cycle and Associated Redox Processes through Time. *Phil.*
741 *Trans. R. Soc. B* **2006**, 361 (1470), 931–950. <https://doi.org/10.1098/rstb.2006.1840>.
- 742

- (22) Bristow, T. F.; Kennedy, M. J.; Derkowski, A.; Droser, M. L.; Jiang, G.; Creaser, R. A. Mineralogical Constraints on the Paleoenvironments of the Ediacaran Doushantuo Formation. *Proceedings of the National Academy of Sciences* **2009**, *106* (32), 13190–13195. <https://doi.org/10.1073/pnas.0901080106>.
- (23) Higgins, J. A.; Blättler, C. L.; Lundstrom, E. A.; Santiago-Ramos, D. P.; Akhtar, A. A.; Crüger Ahm, A.-S.; Bialik, O.; Holmden, C.; Bradbury, H.; Murray, S. T.; et al. Mineralogy, Early Marine Diagenesis, and the Chemistry of Shallow-Water Carbonate Sediments. *Geochimica et Cosmochimica Acta* **2018**, *220*, 512–534. <https://doi.org/10.1016/j.gca.2017.09.046>.
- (24) Huang, J.; Chu, X.; Lyons, T. W.; Planavsky, N. J.; Wen, H. A New Look at Saponite Formation and Its Implications for Early Animal Records in the Ediacaran of South China. *Geobiology* **2013**, *11* (1), 3–14. <https://doi.org/10.1111/gbi.12018>.
- (25) Chitale, V. D.; Alabi, G.; Gramin, P.; Lepley, S.; Piccoli, L. Reservoir Characterization Challenges Due to the Multiscale Spatial Heterogeneity in the Presalt Carbonate Sag Formation, North Campos Basin, Brazil. *Petrophysics* **2015**, *56* (06), 552–576.
- (26) Thompson, D. L.; Stilwell, J. D.; Hall, M. Lacustrine Carbonate Reservoirs from Early Cretaceous Rift Lakes of Western Gondwana: Pre-Salt Coquinas of Brazil and West Africa. *Gondwana Research* **2015**, *28* (1), 26–51. <https://doi.org/10.1016/j.gr.2014.12.005>.
- (27) Tosca, N. J.; Wright, V. P. Diagenetic Pathways Linked to Labile Mg-Clays in Lacustrine Carbonate Reservoirs: A Model for the Origin of Secondary Porosity in the Cretaceous Pre-Salt Barra Velha Formation, Offshore Brazil. *Geological Society, London, Special Publications* **2018**, *435* (1), 33–46. <https://doi.org/10.1144/SP435.1>.
- (28) Saller, A.; Rushton, S.; Buambua, L.; Inman, K.; McNeil, R.; Dickson, J. A. D. (Tony). Presalt Stratigraphy and Depositional Systems in the Kwanza Basin, Offshore Angola. *Bulletin* **2016**, *100* (07), 1135–1164. <https://doi.org/10.1306/02111615216>.
- (29) Wright, V. P.; Barnett, A. J. An Abiotic Model for the Development of Textures in Some South Atlantic Early Cretaceous Lacustrine Carbonates. *Geological Society, London, Special Publications* **2015**, *418* (1), 209–219. <https://doi.org/10.1144/SP418.3>.
- (30) Tutolo, B. M.; Tosca, N. J. Experimental Examination of the Mg-Silicate-Carbonate System at Ambient Temperature: Implications for Alkaline Chemical Sedimentation and Lacustrine Carbonate Formation. *Geochimica et Cosmochimica Acta* **2018**, *225*, 80–101. <https://doi.org/10.1016/j.gca.2018.01.019>.
- (31) White, R.; McKenzie, D. Magmatism at Rift Zones: The Generation of Volcanic Continental Margins and Flood Basalts. *J. Geophys. Res.* **1989**, *94* (B6), 7685. <https://doi.org/10.1029/JB094iB06p07685>.
- (32) Wilson, M. Magmatism and Continental Rifting during the Opening of the South Atlantic Ocean: A Consequence of Lower Cretaceous Super-Plume Activity? *Geological Society, London, Special Publications* **1992**, *68* (1), 241–255. <https://doi.org/10.1144/GSL.SP.1992.068.01.15>.
- (33) Milesi, V. P.; Jézéquel, D.; Debure, M.; Cadeau, P.; Guyot, F.; Sarazin, G.; Claret, F.; Vennin, E.; Chaduteau, C.; Virgone, A.; et al. Formation of Magnesium-Smectite during Lacustrine Carbonates Early Diagenesis: Study Case of the Volcanic Crater Lake Dziani Dzaha (Mayotte - Indian Ocean). *Sedimentology* **2019**, *66* (3), 983–1001. <https://doi.org/10.1111/sed.12531>.
- (34) Irwin, H.; Curtis, C.; Coleman, M. Isotopic Evidence for Source of Diagenetic Carbonates Formed during Burial of Organic-Rich Sediments. *Nature* **1977**, *269* (5625), 209–213. <https://doi.org/10.1038/269209a0>.
- (35) Coltorti, M.; Bonadiman, C.; Hinton, R. W.; Siena, F.; Upton, B. G. J. Carbonatite Metasomatism of the Oceanic Upper Mantle: Evidence from Clinopyroxenes and Glasses in Ultramafic Xenoliths of Grande Comore, Indian Ocean. *Journal of Petrology* **1999**, *40* (1), 133–165. <https://doi.org/10.1093/petroj/40.1.133>.
- (36) Pelleter, A.-A.; Caroff, M.; Cordier, C.; Bachelery, P.; Nehlig, P.; Debeuf, D.; Arnaud, N. Melilite-Bearing Lavas in Mayotte (France): An Insight into the Mantle Source below the Comores. *Lithos* **2014**, *208–209*, 281–297. <https://doi.org/10.1016/j.lithos.2014.09.012>.
- (37) Zinke, J.; Reijmer, J. J. G.; Thomassin, B. A. Systems Tracts Sedimentology in the Lagoon of Mayotte Associated with the Holocene Transgression. *Sedimentary Geology* **2003**, *160* (1–3), 57–79. [https://doi.org/10.1016/S0037-0738\(02\)00336-6](https://doi.org/10.1016/S0037-0738(02)00336-6).
- (38) Gérard, E.; De Goeys, S.; Hugoni, M.; Agogué, H.; Richard, L.; Milesi, V.; Guyot, F.; Lecourt, L.; Borensztajn, S.; Joseph, M.-B.; et al. Key Role of Alphaproteobacteria and Cyanobacteria in the Formation of Stromatolites of Lake Dziani Dzaha (Mayotte, Western Indian Ocean). *Front. Microbiol.* **2018**, *9*, 796. <https://doi.org/10.3389/fmicb.2018.00796>.
- (39) Leboulanger, C.; Agogué, H.; Bernard, C.; Bouvy, M.; Carré, C.; Cellamare, M.; Duval, C.; Fouilland, E.; Got, P.; Intertaglia, L.; et al. Microbial Diversity and Cyanobacterial Production in Dziani Dzaha Crater Lake, a Unique Tropical Thalassohaline Environment. *PLoS ONE* **2017**, *12* (1), e0168879. <https://doi.org/10.1371/journal.pone.0168879>.

- (40) Lewis Jr, W. M. Global Primary Production of Lakes: 19th Baldi Memorial Lecture. *Inland Waters* **2011**, 1 (1), 1–28.
- (41) Mook, W. G.; van der Plicht, J. Reporting ¹⁴C Activities and Concentrations. *Radiocarbon* **1999**, 41 (3), 227–239. <https://doi.org/10.1017/S0033822200057106>.
- (42) Stuiver, M.; Polach, H. A. Discussion Reporting of ¹⁴C Data. *Radiocarbon* **1977**, 19 (3), 355–363. <https://doi.org/10.1017/S0033822200003672>.
- (43) Stuiver, M. Workshop On ¹⁴C Data Reporting. *Radiocarbon* **1980**, 22 (3), 964–966. <https://doi.org/10.1017/S0033822200010389>.
- (44) Bard, E.; Tuna, T.; Fagault, Y.; Bonvalot, L.; Wacker, L.; Fahrni, S.; Synal, H.-A. AixMICADAS, the Accelerator Mass Spectrometer Dedicated to ¹⁴C Recently Installed in Aix-En-Provence, France. *Nuclear Instruments and Methods in Physics Research Section B: Beam Interactions with Materials and Atoms* **2015**, 361, 80–86. <https://doi.org/10.1016/j.nimb.2015.01.075>.
- (45) Capano, M.; Miramont, C.; Guibal, F.; Kromer, B.; Tuna, T.; Fagault, Y.; Bard, E. Wood ¹⁴C Dating with AixMICADAS: Methods and Application to Tree-Ring Sequences from the Younger Dryas Event in the Southern French Alps. *Radiocarbon* **2018**, 60 (1), 51–74. <https://doi.org/10.1017/RDC.2017.83>.
- (46) Reimer, P. J.; Brown, T. A.; Reimer, R. W. Discussion: Reporting and Calibration of Post-Bomb ¹⁴C Data. *Radiocarbon* **2004**, 46 (3), 1299–1304. <https://doi.org/10.1017/S0033822200033154>.
- (47) Vanderplight, J.; Hogg, A. A Note on Reporting Radiocarbon. *Quaternary Geochronology* **2006**, 1 (4), 237–240. <https://doi.org/10.1016/j.quageo.2006.07.001>.
- (48) Steefel, C. I.; Appelo, C. A. J.; Arora, B.; Jacques, D.; Kalbacher, T.; Kolditz, O.; Lagneau, V.; Lichtner, P. C.; Mayer, K. U.; Meeussen, J. C. L.; et al. Reactive Transport Codes for Subsurface Environmental Simulation. *Comput Geosci* **2015**, 19 (3), 445–478. <https://doi.org/10.1007/s10596-014-9443-x>.
- (49) Connolly, J. A. D. The Mechanics of Metamorphic Fluid Expulsion. *Elements* **2010**, 6 (3), 165–172. <https://doi.org/10.2113/gselements.6.3.165>.
- (50) Lasaga, A. C. Rate Laws of Chemical Reactions. *Rev. Mineral. (United States)* **1981**, 8.
- (51) Lasaga, A. C. Chemical Kinetics of Water-Rock Interactions. *J. Geophys. Res.* **1984**, 89 (B6), 4009–4025. <https://doi.org/10.1029/JB089iB06p04009>.
- (52) Aagaard, P.; Helgeson, H. C. Thermodynamic and Kinetic Constraints on Reaction Rates among Minerals and Aqueous Solutions; I, Theoretical Considerations. *American Journal of Science* **1982**, 282 (3), 237–285. <https://doi.org/10.2475/ajs.282.3.237>.
- (53) Burch, T. E.; Nagy, K. L.; Lasaga, A. C. Free Energy Dependence of Albite Dissolution Kinetics at 80°C and PH 8.8. *Chemical Geology* **1993**, 105 (1–3), 137–162. [https://doi.org/10.1016/0009-2541\(93\)90123-Z](https://doi.org/10.1016/0009-2541(93)90123-Z).
- (54) Regnier, P.; Steefel, C. I. A High Resolution Estimate of the Inorganic Nitrogen Flux from the Scheldt Estuary to the Coastal North Sea during a Nitrogen-Limited Algal Bloom, Spring 1995. *Geochimica et Cosmochimica Acta* **1999**, 63 (9), 1359–1374. [https://doi.org/10.1016/S0016-7037\(99\)00034-4](https://doi.org/10.1016/S0016-7037(99)00034-4).
- (55) Pennell, K. D.; Abriola, L. M.; Boyd, S. A. Surface Area of Soil Organic Matter Reexamined. *Soil Science Society of America Journal* **1995**, 59 (4), 1012. <https://doi.org/10.2136/sssaj1995.03615995005900040008x>.
- (56) Robie, R. A.; Hemingway, B. S. *Thermodynamic Properties of Minerals and Related Substances at 298.15 K and 1 Bar (105 Pascals) Pressure and at Higher Temperatures*; US Government Printing Office, 1995; Vol. 2131.
- (57) Brantley, S. L.; Mellott, N. P. Surface Area and Porosity of Primary Silicate Minerals. *American Mineralogist* **2000**, 85 (11–12), 1767–1783. <https://doi.org/10.2138/am-2000-11-1220>.
- (58) Helgeson, H. C. Summary and Critique of the Thermodynamic Properties of Rock-Forming Minerals. *American Journal of Science* **1978**, 278, 1–229.
- (59) Knauss, K. G.; Nguyen, S. N.; Weed, H. C. Diopside Dissolution Kinetics as a Function of PH, CO₂, Temperature, and Time. *Geochimica et Cosmochimica Acta* **1993**, 57 (2), 285–294. [https://doi.org/10.1016/0016-7037\(93\)90431-U](https://doi.org/10.1016/0016-7037(93)90431-U).
- (60) Richet, P.; Bottinga, Y.; Denielou, L.; Petitet, J. P.; Tequi, C. Thermodynamic Properties of Quartz, Cristobalite and Amorphous SiO₂: Drop Calorimetry Measurements between 1000 and 1800 K and a Review from 0 to 2000 K. *Geochimica et Cosmochimica Acta* **1982**, 46 (12), 2639–2658. [https://doi.org/10.1016/0016-7037\(82\)90383-0](https://doi.org/10.1016/0016-7037(82)90383-0).
- (61) Pokrovskii, V. A.; Helgeson, H. C. Thermodynamic Properties of Aqueous Species and the Solubilities of Minerals at High Pressures and Temperatures: The System Al₂O₃-H₂O-KOH. *Chemical Geology* **1997**, 137 (3–4), 221–242. [https://doi.org/10.1016/S0009-2541\(96\)00167-2](https://doi.org/10.1016/S0009-2541(96)00167-2).
- (62) Medvedev, V. A.; Cox, J. D.; Wagman, D. D. *CODATA Key Values for Thermodynamics*; Hemisphere Publishing Corporation New York, 1989.

- 860 (63) Cubillas, P.; Köhler, S.; Prieto, M.; Chaïrat, C.; Oelkers, E. H. Experimental Determination of the
861 Dissolution Rates of Calcite, Aragonite, and Bivalves. *Chemical Geology* **2005**, *216* (1–2), 59–77.
862 <https://doi.org/10.1016/j.chemgeo.2004.11.009>.
- 863 (64) Romanek, C. S.; Grossman, E. L.; Morse, J. W. Carbon Isotopic Fractionation in Synthetic Aragonite
864 and Calcite: Effects of Temperature and Precipitation Rate. *Geochimica et Cosmochimica Acta* **1992**, *56*
865 (1), 419–430. [https://doi.org/10.1016/0016-7037\(92\)90142-6](https://doi.org/10.1016/0016-7037(92)90142-6).
- 866 (65) Busenberg, E.; Plummer, L. N.; Mumpston, F. A. A Comparative Study of the Dissolution and Crystal
867 Growth Kinetics of Calcite and Aragonite. *Studies Diagenesis USGS Bull* **1986**, *1578*, 139–168.
- 868 (66) Königsberger, E.; Königsberger, L.-C.; Gamsjäger, H. Low-Temperature Thermodynamic Model for the
869 System Na₂CO₃–MgCO₃–CaCO₃–H₂O. *Geochimica et Cosmochimica Acta* **1999**, *63* (19–20), 3105–
870 3119. [https://doi.org/10.1016/S0016-7037\(99\)00238-0](https://doi.org/10.1016/S0016-7037(99)00238-0).
- 871 (67) Gautier, Q.; Bénézeth, P.; Mavromatis, V.; Schott, J. Hydromagnesite Solubility Product and Growth
872 Kinetics in Aqueous Solution from 25 to 75°C. *Geochimica et Cosmochimica Acta* **2014**, *138*, 1–20.
873 <https://doi.org/10.1016/j.gca.2014.03.044>.
- 874 (68) Vicente, M. A.; Suárez, M.; López-González, J. de D.; Bañares-Muñoz, M. A. Characterization, Surface
875 Area, and Porosity Analyses of the Solids Obtained by Acid Leaching of a Saponite. *Langmuir* **1996**, *12*
876 (2), 566–572. <https://doi.org/10.1021/la950501b>.
- 877 (69) Kooli, F.; Jones, W. Characterization and Catalytic Properties of a Saponite Clay Modified by Acid
878 Activation. *Clay miner.* **1997**, *32* (4), 633–643. <https://doi.org/10.1180/claymin.1997.032.4.13>.
- 879 (70) Suárez Barrios, M.; de Santiago Buey, C.; García Romero, E.; Martín Pozas, J. M. Textural and
880 Structural Modifications of Saponite from Cerro Del Aguila by Acid Treatment. *Clay miner.* **2001**, *36*
881 (4), 483–488. <https://doi.org/10.1180/0009855013640003>.
- 882 (71) Steudel, A.; Friedrich, F.; Schuhmann, R.; Ruf, F.; Sohling, U.; Emmerich, K. Characterization of a
883 Fine-Grained Interstratification of Turbostratic Talc and Saponite. *Minerals* **2017**, *7* (1), 5.
884 <https://doi.org/10.3390/min7010005>.
- 885 (72) Whitticar, M. J. Carbon and Hydrogen Isotope Systematics of Bacterial Formation and Oxidation of
886 Methane. *Chemical Geology* **1999**, *161* (1–3), 291–314. [https://doi.org/10.1016/S0009-2541\(99\)00092-3](https://doi.org/10.1016/S0009-2541(99)00092-3).
- 887 (73) Etiope, G.; Sherwood Lollar, B. Abiotic Methane on Earth. *Rev. Geophys.* **2013**, *51* (2), 276–299.
888 <https://doi.org/10.1002/rog.20011>.
- 889 (74) Albéric, P.; Jézéquel, D.; Bergonzini, L.; Chapron, E.; Viollier, E.; Massault, M.; Michard, G. Carbon
890 Cycling and Organic Radiocarbon Reservoir Effect in a Meromictic Crater Lake (Lac Pavin, Puy-de-
891 Dôme, France). *Radiocarbon* **2013**, *55* (2), 1029–1042. <https://doi.org/10.1017/S0033822200058161>.
- 892 (75) Hua, Q.; Barbetti, M.; Rakowski, A. Z. Atmospheric Radiocarbon for the Period 1950–2010.
893 *Radiocarbon* **2013**, *55* (4), 2059–2072. https://doi.org/10.2458/azu_js_rc.v55i2.16177.
- 894 (76) Canfield, D. E.; Kristensen, E.; Thamdrup, B. *Aquatic Geomicrobiology*; Gulf Professional Publishing,
895 2005.
- 896 (77) Sayles, F. L.; Fyfe, W. S. The Crystallization of Magnesite from Aqueous Solution. *Geochimica et*
897 *Cosmochimica Acta* **1973**, *37* (1), 87–99. [https://doi.org/10.1016/0016-7037\(73\)90246-9](https://doi.org/10.1016/0016-7037(73)90246-9).
- 898 (78) Arvidson, R. S. The Dolomite Problem; Control of Precipitation Kinetics by Temperature and Saturation
899 State. *American Journal of Science* **1999**, *299* (4), 257–288. <https://doi.org/10.2475/ajs.299.4.257>.
- 900 (79) Baker, P. A.; Kastner, M. Constraints on the Formation of Sedimentary Dolomite. *Science* **1981**, *213*
901 (4504), 214–216. <https://doi.org/10.1126/science.213.4504.214>.
- 902 (80) Meunier, A. *Clays*; Springer Science & Business Media, 2005.
- 903 (81) Tosca, N. Geochemical Pathways to Mg-Silicate Formation. *Magnesian Clays: Characterization, Origin*
904 *and Applications*; Pozo, M., Galán, E., Eds **2015**, 283–329.
- 905 (82) Parkhurst, D. L.; Appelo, C. A. J. *Description of Input and Examples for PHREEQC Version 3: A*
906 *Computer Program for Speciation, Batch-Reaction, One-Dimensional Transport, and Inverse*
907 *Geochemical Calculations*; US Geological Survey, 2013.
- 908 (83) Stoessell, R. K. 25°C and 1 Atm Dissolution Experiments of Sepiolite and Kerolite. *Geochimica et*
909 *Cosmochimica Acta* **1988**, *52* (2), 365–374. [https://doi.org/10.1016/0016-7037\(88\)90092-0](https://doi.org/10.1016/0016-7037(88)90092-0).
- 910 (84) Ali, A. D.; Tuner, P. Authigenic K-Feldspar in the Bromsgrove Sandstone Formation (Triassic) of
911 Cntral England. *Journal of Sedimentary Research* **1982**, *52* (1), 187–197.
912 <https://doi.org/10.1306/212F7F09-2B24-11D7-8648000102C1865D>.
- 913 (85) Per Arne Bjorkum, Norvald Gjelsvik. An Isochemical Model for Formation of Authigenic Kaolinite, K-
914 Feldspar and Illite in Sediments. *SEPM JSR* **1988**, Vol. 58. <https://doi.org/10.1306/212F8DD2-2B24-11D7-8648000102C1865D>.
- 915 (86) Druhan, J. L.; Steefel, C. I.; Molins, S.; Williams, K. H.; Conrad, M. E.; DePaolo, D. J. Timing the Onset
916 of Sulfate Reduction over Multiple Subsurface Acetate Amendments by Measurement and Modeling of
917 Sulfur Isotope Fractionation. *Environ. Sci. Technol.* **2012**, *46* (16), 8895–8902.
918 <https://doi.org/10.1021/es302016p>.
- 919

- (87) Rehim, H.; Pimentel, A. M.; Carvalho, M. D.; Monteiro, M. Talco e Estevensita Na Formação Lagoa Feia Da Bacia de Campos-Possíveis Implicações No Ambiente Depositional. In *Anais XXXIV Congresso Brasileiro de Geologia*; 1986; Vol. 1, pp 416–422.
- (88) Cerling, T. E. Chemistry of Closed Basin Lake Waters: A Comparison between African Rift Valley and Some Central North American Rivers and Lakes. *The Global Geological Record of Lake Basins* **1994**, *1*, 29–30.
- (89) Balthasar, U.; Cusack, M. Aragonite-Calcite Seas—Quantifying the Gray Area. *Geology* **2015**, *43* (2), 99–102. <https://doi.org/10.1130/G36293.1>.
- (90) Rossi, C.; Lozano, R. P. Hydrochemical Controls on Aragonite versus Calcite Precipitation in Cave Dripwaters. *Geochimica et Cosmochimica Acta* **2016**, *192*, 70–96. <https://doi.org/10.1016/j.gca.2016.07.021>.
- (91) Zeyen, N.; Daval, D.; Lopez-Garcia, P.; Moreira, D.; Gaillardet, J.; Benzerara, K. Geochemical Conditions Allowing the Formation of Modern Lacustrine Microbialites. *Procedia Earth and Planetary Science* **2017**, *17*, 380–383. <https://doi.org/10.1016/j.proeps.2016.12.096>.
- (92) Torsvik, T. H.; Rousse, S.; Labails, C.; Smethurst, M. A. A New Scheme for the Opening of the South Atlantic Ocean and the Dissection of an Aptian Salt Basin. *Geophysical Journal International* **2009**, *177* (3), 1315–1333. <https://doi.org/10.1111/j.1365-246X.2009.04137.x>.
- (93) Teboul, P.-A.; Kluska, J.-M.; Marty, N. C. M.; Debure, M.; Durlet, C.; Virgone, A.; Gaucher, E. C. Volcanic Rock Alterations of the Kwanza Basin, Offshore Angola - Insights from an Integrated Petrological, Geochemical and Numerical Approach. *Marine and Petroleum Geology* **2017**, *80*, 394–411. <https://doi.org/10.1016/j.marpetgeo.2016.12.020>.



942

943 FOR TOC GRAPHIC USE ONLY

944